JGR Oceans

RESEARCH ARTICLE
10.1029/2021JC017661

Long-Distance/Time Surf-Zone Tracer Evolution Affected by Inner-Shelf Tracer Retention and Recirculation

D. J. Grimes[1], F. Feddersen[2], and S. N. Giddings[2]

[1]University of North Carolina Wilmington, Wilmington, NC, USA, [2]Scripps Institution of Oceanography, University of California San Diego, La Jolla, CA, USA

Key Points:

- Tracer evolution from a 3.8 hr surfzone release was observed for ≈30 hr and ≈7 km alongshore
- Surfzone alongshore tracer transport and exchange with inner-shelf lead to surf-zone tracer decay and skewed timeseries farther downstream
- A coupled surfzone/inner-shelf tracer model quantifies how inner-shelf retention and recirculation are key to surfzone tracer evolution

Correspondence to:
D. J. Grimes,
grimesdj@uncw.edu

Citation:
Grimes, D. J., Feddersen, F., & Giddings, S. N. (2021). Long-distance/time surf-zone tracer evolution affected by inner-shelf tracer retention and recirculation. *Journal of Geophysical Research: Oceans*, *126*, e2021JC017661. https://doi.org/10.1029/2021JC017661

Received 16 JUN 2021
Accepted 25 OCT 2021

Abstract The evolution of a surf-zone released tracer (≈100 Liter over 4 hr) was observed for ≈30 h. Surf-zone tracer was transported alongshore (y) with relatively steady mean speed $v_{SZ} \approx 0.18$ m s^{-1}, consistent with obliquely incident wave forcing. Maximum *in situ* surf-zone tracer concentration decayed exponentially with 1.6 km alongshore e-folding length scale, that is, 2.5 hr advective time scale. Surf-zone tracer time-series evolved downstream of the release from a top-hat structure for $y \leq 1$ km to increasingly skewed farther downstream. Within ≈1.5 km of the northward propagating tracer front, inner-shelf tracer was confined to onshore of $\approx 4L_{SZ}$ (surf-zone width $L_{SZ} \approx 100$ m) and was alongshore patchy. A coupled surf-zone/inner-shelf tracer advection-diffusion-exchange box model reproduces the observed surf-zone downstream max concentration decay and temporal skewness, with surf-zone flushing time $k_{SZ}^{-1} \approx 2.3$ h. A weaker inner-shelf unidirectional-exchange rate $k_{IS} \approx k_{SZ}/2$ indicates reduced horizontal mixing outside the surf-zone. Surf-zone temporal skewness is linked to inner-shelf tracer storage, differential surf-zone/inner-shelf advection, and recirculation, that is, non-asymptotic shear dispersion. On the inner-shelf ($\approx 3L_{SZ}$), tracer vertical structure differed in the morning versus afternoon suggesting internal tide and solar forced thermal modulation. Model parameters representing surf-zone processes are well constrained by existing observations and scales. However, the many overlapping inner-shelf processes make a single process based generalization of inner-shelf cross-shore exchange rate (i.e., k_{IS}) and alongshore transport difficult.

Plain Language Summary Transport and mixing impact nearshore systems, such as larval recruitment in intertidal ecosystems and water quality impacts from coastal pollution, and can be studied using shoreline released tracers, like fluorescent dye. In the region of depth-limited wave breaking, the surf-zone, alongshore directed currents driven by oblique breaking waves transport tracers over long distances. Tracer is also mixed across the surf-zone by eddying currents and exported onto the inner-shelf (region offshore of the surf-zone) by rip currents, which decreases shoreline tracer concentration. Horizontal mixing also increases tracer plume length-scales, known as dispersion, and cross-shore variation in the alongshore current can induce enhanced alongshore dispersion. Over long-distances/times, tracer evolution depends on both surf-zone and inner-shelf currents and alongshore dispersion. Here, the evolution of a surf-zone released dye tracer is observed for ≈30 h and over several kilometers downstream (alongshore). Downstream of the release, the surf-zone maximum concentration decayed and concentration time-series developed long-duration tails (skewness). A surf-zone/inner-shelf box model reproduces the surf-zone tracer observations, providing insight to the relative roles of cross-shore exchange, recirculation and alongshore dispersion. Importantly, recirculation between the surf-zone and the inner-shelf is a critical process that changes the tracer distribution close to shore.

1. Introduction

The transport and dilution of shoreline released tracers, such as pathogens (e.g., Boehm, 2003) or larvae (e.g., Morgan et al., 2018), is important to coastal ecosystems and human health (Boehm et al., 2017). The surf-zone can entrain shoreline released tracers and discharges from small-scale and low-flow rivers, estuaries and out-falls (Kastner et al., 2019; Rodriguez et al., 2018; Wong et al., 2013). Surf-zone released tracers have been detected in coastal community aerosols (Pendergraft et al., 2021), indicating potential for pathogen and toxin exposure without direct coastal water contact (e.g., Kirkpatrick et al., 2010). On alongshore uniform beaches, surf-zone alongshore (y) currents, driven by obliquely incident surface gravity wave forcing (e.g., Feddersen et al., 1998; Lentz et al., 1999; Longuet-Higgins, 1970), transport tracers over long $\mathcal{O}(10$ km) distances (e.g., Feddersen et al., 2016; Grimes, Feddersen, Giddings, & Pawlak, 2020; Grant et al., 2005), increasing the potential for human health impacts of pollution beyond a point source location. However, despite the societal relevance, surf-zone

tracer evolution (transport and dilution) over >1 km alongshore scales and the role of surf-zone/inner-shelf exchange and inner-shelf processes are not well understood.

Surf-zone tracer evolution has been studied using either instantaneous shoreline releases (e.g., Brown et al., 2019; Clarke et al., 2007; Harris et al., 1963), or continuous releases (e.g., Clark et al., 2010; Hally-Rosendahl et al., 2014, 2015). Quantitative analysis of *in situ* surf-zone tracer concentration D has been restricted to alongshore (y) distances of 10–100 m (Clark et al., 2010; Brown et al., 2019) to ≈ 1 km (Hally-Rosendahl et al., 2014, 2015), representing advective-time scales (t) from 1 min to 1 hr after release, that is, $t \sim y/v_{SZ}$, given quasi-steady mean alongshore current v_{SZ}. On an alongshore uniform dissipative beach with $v_{SZ} \sim 0.25$ m s^{-1}, continuously released tracer was surf-zone confined within 200 m downstream (≈15 min) and the observed surf-zone cross-shore (x) ensemble-mean tracer dispersion was Fickian, exhibiting down-mean-gradient diffusive flux with constant diffusion coefficient (e.g., Clark et al., 2010). The $\mathcal{O}(1\ \text{m}^2\ \text{s}^{-1})$ cross-shore diffusivity was related to horizontal surf-zone eddies, that is, vertical vorticity, and resulted in a power-law alongshore decay in maximum surf-zone concentration $D_{max} \sim y^{-1/2}$ (Clark et al., 2010). Under similar wave and surf-zone conditions, but over larger downstream distance ($0.1 \le y \le 1$ km), substantially weaker shoreline $D_{max}(y)$ alongshore power-law decay (non-Fickian) was observed due to inner-shelf tracer build-up and recirculation (Hally-Rosendahl et al., 2014, 2015). Observations on a reflective beach are qualitatively similar to dissipative beaches, but with the surf-zone becoming well mixed over shorter length/time scales, for example, within 25 m alongshore or 5 min ($v_{SZ} \approx 0.8$ m s^{-1}) of the release, due to the narrower surf-zone (Brown et al., 2019). Long-range tracer dispersion is likely non-Fickian due to differences in surf-zone and inner-shelf hydrodynamics and diffusivity. However, quantitative *in situ* D observations on dissipative beaches over scales >1 km and >1 h are lacking.

At fixed downstream distances from an instantaneous release, D time-series typically exhibit temporal skewness, having relatively steep D growth, and increasingly gradual signal decay (Brown et al., 2019; Clarke et al., 2007; Harris et al., 1963), similar to tracer release observations in rivers (cf. Young & Jones, 1991). Continuous mixing causes downstream decreasing peak concentration and increasing temporal width, indicating a growing alongshore plume width (Harris et al., 1963). On rip-channeled bathymetries, mean circulation tends to recirculate and surf-zone trap floating material in models and observations (Brown et al., 2015; Geiman et al., 2011; Reniers et al., 2009), whereas intermittent rip-current pulses eject material farther offshore (Reniers et al., 2010). Over short alongshore distances ($y \le 100$ m), rip-current cell retention and recirculation can prolong surf-zone tracer signal (e.g., Clarke et al., 2007). After terminating the dye release, Hally-Rosendahl et al. (2014) observed very slow surf-zone D decay (> 8 h) at $\tilde{y} \approx 500$ m, likely due to recirculation of inner-shelf dye because of the short surf-zone advective time-scale ($y/v_{SZ} \approx 1$ hr, with $v_{SZ} \approx 0.15$ m s^{-1}) and weak inner-shelf alongshore current ($v_{IS} \approx 0$). Quantitative analysis of surf-zone/inner-shelf exchange, recirculation and differential alongshore transport on scales $y > 1$ km and $t > 10$ hr has not been conducted.

Inner-shelf tracer retention and subsequent surf-zone recirculation is partly due to the cross-shore distribution of the horizontal eddies responsible for mixing. As breaking wave vorticity forcing is confined to the surf-zone (Clark et al., 2012; Peregrine, 1998), inner-shelf horizontal eddies predominately originate from the surf-zone via transient rip current ejections (e.g., Feddersen, 2014; Johnson & Pattiaratchi, 2006). Transient rip currents (TRC) are characterized by concentrated and ephemeral offshore flows that trap and advect surf-zone tracers (e.g., dye and temperature) onto the inner-shelf, resulting in an alongshore patchy inner-shelf tracer field (e.g., Hally-Rosendahl et al., 2014). The strength of TRC-induced surf-zone to inner-shelf exchange is commonly quantified using an exchange velocity (u_{EX}, e.g., Hally-Rosendahl et al., 2015). In wave-resolving Boussinesq simulations, TRC-induced horizontal eddy velocities have self-similar cross-shore decay, depending on incident wave and beach slope parameters (Suanda & Feddersen, 2015). Inner-shelf eddy variability, within ≈5L_{SZ} of shore, is also increased in models that include wave averaged surf-zone dynamics, relative to models that do not include a surf-zone (Wu et al., 2021). Cross-shore inhomogeneous mixing due to surf-zone generated horizontal coherent eddies results in reduced dispersion of surf-zone released tracer on the inner-shelf (Spydell et al., 2019).

Shoreline released tracer plumes often exhibit strong anisotropic growth, tending to form wide alongshore $\mathcal{O}$(10 km) and narrow cross-shore $\mathcal{O}$(500 m) shoreline connected plumes (Feddersen et al., 2016; Grant et al., 2005). Predominate alongshore widening (spreading) is commonly ascribed to shear induced dispersion. Over relatively short duration (<1 h) surf-zone drifter releases, strong intra-surf-zone alonshore current shear resulted in enhanced alongshore diffusivity $K_{yy} \sim v_{SZ}^2 \tau_L = \mathcal{O}(1 - 10\,\text{m}^2\,\text{s}^{-1})$, with Lagrangian time-scale $\tau_L = \mathcal{O}(1 - 10\,\text{min})$, analogous to asymptotic shear dispersion in pipe- and channel-flows (Spydell et al., 2009).

For large scale plumes, where tracer is both in the surf-zone and on the inner-shelf (e.g., Feddersen et al., 2016; Grant et al., 2005), alongshore diffusivity estimates based on the reported plume evolution imply significantly larger alongshore diffusivities $\mathcal{O}(10-100\,\mathrm{m^2\,s^{-1}})$.

Alongshore momentum dynamics vary across the surf-zone and inner-shelf, and alongshore currents can be strongly sheared (e.g., Lentz et al., 1999). Inner-shelf alongshore momentum dynamics also differ from the surf-zone, with dominant contributions from wind and waves (e.g., Austin & Lentz, 2002; Lentz & Fewings, 2012), and alongshore pressure gradients (Wu et al., 2020). Under realistic conditions, numerous processes affect inner-shelf tracer evolution (e.g., Fong & Stacey, 2003; Jones et al., 2008), including internal waves (e.g., Moniz et al., 2014; Sundermeyer & Ledwell, 2001), baroclinic circulation (e.g., Grimes, Feddersen & Kumar, 2020; Kumar & Feddersen, 2017; Molina et al., 2014; Moulton et al., 2021), and cross-shore oriented coastal sub-mesoscale fronts (e.g., Wu et al., 2020). However, limited observations from surf-zone dye release experiments suggest inner-shelf mixing is weaker than in the surf-zone (e.g., Brown et al., 2019, among others; Clark et al., 2010). As larger scale plumes involve both surf-zone and inner-shelf tracer evolution, cross-shore inhomogeneous horizontal mixing (differing surf-zone/inner-shelf turbulence) combined with surf-zone/inner-shelf alongshore current shear potentially induce a form of enhanced inter-surf-zone/inner-shelf shear dispersion. However, lack of quantitative field measurements of tracer evolution at these time/space scales previously prevented a detailed assessment of this mechanism.

Here, observations from a finite duration surf-zone tracer release experiment are analyzed to quantify the role of surf-zone/inner-shelf exchange, recirculation, and shear dispersion over relatively long ≈ 30 h time and 7 km space scales. The field site, experimental methods, remote and *in situ* observational instrumentation and processing are described in Section 2. Experiment environmental conditions and detailed tracer observations are presented in Section 3. In Section 4, a coupled surf-zone/inner-shelf box tracer model is developed and model parameters optimized based on surf-zone spatiotemporal tracer observations. Model parameters quantify the role of various transport and dispersion mechanisms in the observed tracer evolution. In Section 5, alternative tracer evolution equations are used to elucidate contributions from recirculation and alongshore current shear. Also in Section 5, inner-shelf tracer (dye and temperature) observations are contextualized with recent work highlighting the important role of buoyancy on inner-shelf tracer evolution. Results are summarized in Section 6.

2. Methods

2.1. Study Region and Dye Release

A series of surf-zone tracer releases were conducted in September–October 2015 in southern San Diego, California (Figure 1a) as part of the cross–surf-zone/inner-shelf dye exchange (CSIDE) field study on processes affecting cross-shore tracer exchange and the associated time and space scales at which they operate. Here, tracer evolution is evaluated from a surf-zone release on October 8, 2015, located roughly 1 km North of Imperial Beach (IB). The study domain origin $(x, y) = (0, 0)$ is centered on the surf-zone tracer release (magenta, Figure 1), with the y-coordinate roughly alongshore oriented near the release and to within 1° of true North. The positive upward vertical coordinate is defined with $z = 0$ at mean sea level (MSL). The 3.84 hr duration mid-surf-zone tracer release began early morning, at $t_r = 05{:}18$ PDT, and observations are presented relative to the time since release start $\mathcal{T} = (t - t_r)$ in hours. A total of 113.6 L of 21.49% Rhodamine WT fluorescent dye solution, or total dye mass $M \approx 2.44 \times 10^7$ ppb m^3 (ppb = parts per billion), was pumped via a medical-grade peristaltic pump at a rate of ≈ 0.5 L min^{-1} at a fixed position with water depth 0.5 ± 0.25 m. For reference, uniformly distributing the total dye mass across a 100 m wide surf-zone with constant beach slope of 0.02 and over 2.5 km alongshore would result in a surf-zone concentration of ≈ 98 ppb.

2.1.1. Shorenormal Coordinates

At alongshore scales > 1 km, the coastline curves monotonically from west facing offshore in IB ($x = 0$, $y = -1$ km; Figure 1a) to south facing offshore at the San Diego Bay entrance ($x = -9$, $y = 10$ km). To simplify presentation and analysis, observations are transformed to a quasi-shorenormal coordinate system using the smooth MSL-contour as a baseline. Results are not sensitive to changes in the coordinate transformation details. The 2012 NOAA San Diego, CA 1/3 arc-second coastal digital elevation model (https://www.ncei.noaa.gov/metadata/geoportal/rest/metadata/item/gov.noaa.ngdc.mgg.dem:3542/html#) is first convolved with a 100×100 m^2 Hamming window to remove poorly resolved artifacts from the patch-work data, giving $z = -h(x,$

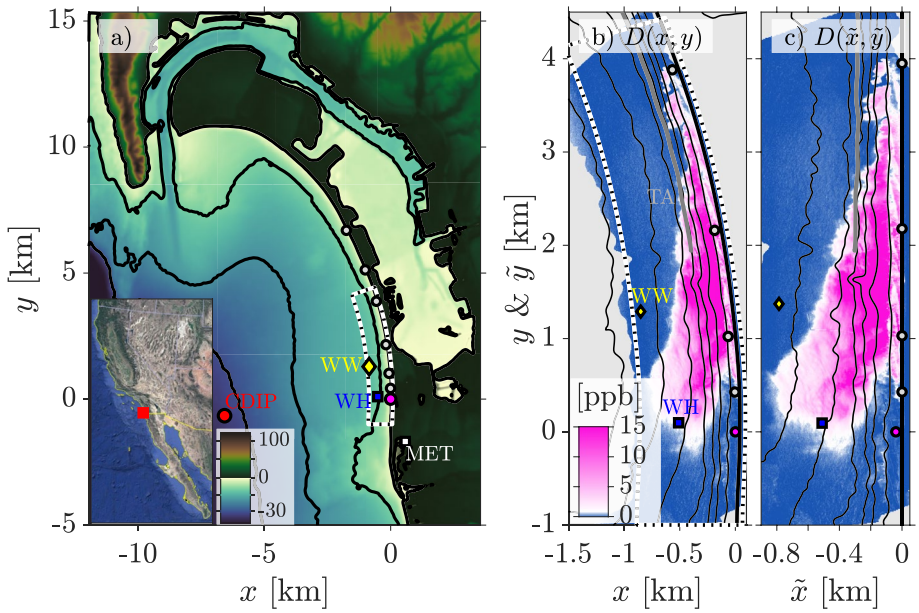

Figure 1. (a) Southern San Diego bight study region topography (green/brown) and bathymetry (blue) with {0, 10, 20, 30 m} depths contoured in black. Also indicated are the surf-zone dye release location $(x, y) = (0, 0)$ (magenta), surf-zone sampling sites (gray dots), Wirewalker array (WW, yellow), RDI Workhorse current meter (WH, blue), Coastal Data Information Program wave buoy 218 (CDIP, red), and Tijuana River National Estuarine Research Reserve meteorological station (MET, white). (b) Example MASS hyperspectral imagery derived surface dye D at $\mathcal{T} = 5.1$ h since release start versus physical coordinates (x, y), and in (c) mapped to quasi-shorenormal coordinates $(\tilde{x}, \tilde{y})$ using the smoothed mean-sea-level contour from (a and b) within the dashed boundary. Also shown in (b and c) is the inner-shelf alongshore towed-array transect (TA, gray). Regions without data are gray and bathymetry contours are drawn at 2 m intervals.

y), the bathymetry (blues, $h \geq 0$) and topography (greens, $h < 0$) shown in Figure 1. The MSL ($h = 0$) contour is extracted within 10 km of the tracer release by linearly interpolating between adjacent points above and below MSL. The resulting discrete column vector of raw MSL coordinates, denoted $(\mathbf{x}_{msl}, \mathbf{y}_{msl})$, has an alongshore resolution of ≈ 10 m and the accompanying alongshore averaged MSL beach slope $\bar{\beta}_{msl} = 0.042$. A second-order Butterworth low-pass filter with ≈ 500 m cutoff is applied to $(\mathbf{x}_{msl}, \mathbf{y}_{msl})$ to remove rhythmic artifacts due to beach cusps, and then interpolated to 2 m alongshore resolution, giving a smooth baseline curve $(\mathbf{x}_b, \mathbf{y}_b)$. The baseline curves west for $y > 0$ with minimum radius of curvature $r_c \approx 6.5$ km.

Observations are mapped from physical space (x, y) to shorenormal coordinates $(\tilde{x}, \tilde{y})$ by first locating the index i of the nearest point on the baseline curve $(\mathbf{x}_b, \mathbf{y}_b)$. The cross-shore coordinate $\tilde{x}$ is taken as minus the distance from (x, y) to $(x_{b,i}, y_{b,i})$, $\tilde{x} = -\|(x, y) - (x_{b,i}, y_{b,i})\|$. The origin of the quasi-shorenormal system $(\tilde{x}, \tilde{y}) = (0, 0)$ corresponds to the point on the baseline curve nearest the tracer release physical location $(x, y) = (0, 0)$, giving transformed release coordinates $\tilde{x} \approx -40$ m and $\tilde{y} = 0$. The along-shore coordinate $\tilde{y}$ is measured as the distance along the baseline from the origin. Alongshore length scales are slightly dilated (< 8% for $\tilde{x} \geq -500$ m) by the transformation due to the MSL curvature. An example of the coordinate mapping applied to remote aerial imagery derived surface dye D is shown in Figures 1b and 1c.

2.2. Data Sources

Various fixed and mobile *in situ* and remote sensing platforms were used to measure experimental physical conditions and tracer evolution. In the surf-zone, dye concentration and temperature were measured at 1-Hz using several Wetlab Eco-Triplet fluorometers and either an internal thermistor or co-mounted Sea-Bird-39 thermistor, respectively. The surf-zone tracer D and temperature T measurements are 30 min bin-averaged and the associated bin-standard deviation are displayed as either shading or error-bars. Surf-zone D is also corrected for bubble and turbidity induced fluorescent signal quenching; the resulting minimum detection level is ≈ 1 ppb (Clark et al., 2009). Surf-zone instruments were moved up/down the beachface over the tidal cycle to maintain

mid-surf-zone position and ensure that sensors remained submerged throughout wave-induced water level changes, which resulted in some low-tide data gaps.

On the inner-shelf, temperature moorings and current meters were deployed in depths varying from 8 to 30 m from early Sept. to mid-Oct. Here, depth-averaged alongshore currents are presented from two acoustic Doppler current profilers (ADCP): a 1.2-MHz RDI-Workhorse 4-beam ADCP in 12 m depth (WH, Figures 1a–1b) and a 1-MHz Nortek Aquadopp 3-beam ADCP adjacent to a Wirewalker wave-powered profiler with Sea-Bird-49 conductivity-temperature-depth sensor in 13 m depth (WW, Figures 1a and 1b). The depth-averaged inner-shelf currents are also low-pass filtered with a 30-min moving window. The WW ADCP pressure record is used to estimate surface water level record $\eta(t)$ by first removing the >1 month mean pressure and then converted from mean-water level elevation to MSL using the nearby NOAA tide-gauge (9410170) in San Diego Bay. Inner-shelf vessel based alongshore T and D transects were conducted using a towed array of 5 Eco-triplets sampling at 1-Hz between 1 and 6 m subsurface (TA, Figures 1b and 1c). The inner-shelf alongshore transect observations are low-pass filtered to remove variability on time-scales <30 s, or <18 m based on the average vessel speed 0.6 m s^{-1}, then linearly interpolated in the vertical between instruments. Surface dye concentration D and relative temperature T' were also measured remotely using the modular aerial sensing system (MASS; Melville et al., 2016). Grimes, Feddersen, Giddings, and Pawlak (2020) give a more detailed description of the full experimental array.

2.3. MASS Processing Algorithms

2.3.1. Remotely Derived Dye Concentration

The MASS hyperspectral imagery is used to estimate near-surface tracer concentration. ∼1 km wide cross-shore by >5 km long alongshore transects were flown every 3–8 min over $5 \leq \mathcal{T} < 12.5$, except for 2 hr mid-day for refueling/resupplying. MASS spectral radiance measurements (denoted $r(\lambda)$ in mW $(\mathrm{cm}^2\ \mathrm{str}\ \mathrm{nm})^{-1}$ from 400 to 990 nm in 126 bands) are first mapped from physical (x, y) to transformed $(\tilde{x}, \tilde{y})$ coordinates and bin-averaged to 10 m alongshore by 2 m cross-shore resolution. Fluorescent tracer intensity (I) is estimated from $r(\lambda)$ using the ratio of the average radiance in the Rhodamine WT fluorescence emission wavelength band $585 \leq \lambda_a \leq 590$ nm to the absorption band $552 \leq \lambda_a \leq 562$ nm,

$$I = \frac{\bar{r}(\lambda_e)}{\bar{r}(\lambda_a)}, \tag{1}$$

where the over-bar implies averaging over the respective wavelength band. The remote intensity $I(x, y, t)$ measurements are calibrated to *in situ* tracer concentration (ppb) using co-aligned near-surface personal water-craft $D(x, y, t)$ measurements. Following Clark et al. (2014), a linear relationship between remote tracer intensity (I) and *in situ* concentration (D) is assumed, that is,

$$D_0(x, y) = m\, I(x, y) + b, \tag{2}$$

where slope (m) and intercept (b) minimize the squared error between personal water-craft D measurements and the remote estimate D_0 averaged over a 7 m radius. As $I(x, y, t)$ is a measure of the fluorescence within the optical depth, there is potential sensitivity to tracer vertical structure, which are not considered here. Hereafter, all references to remotely sensed dye concentration imply a near-surface averaged concentration. The hyperspectral D_0 algorithm (1 and 2) is sensitive to water optical properties (e.g., turbidity) and foam, which vary strongly in the cross-shore (:). A mean cross-shore distribution of background tracer signal is determined using cross-shore $D_0(\tilde{x})$ transects from 17 passes at dye-free alongshore locations. The average background concentration profile, denoted $D_b(\tilde{x})$, is approximately constant at 2.5 ppb in the surf-zone ($\tilde{x} \gtrapprox -100$ m) and rapidly decays to < 0.5 ppb for $\tilde{x} \leq -200$ m (not shown). The alongshore uniform background concentration is removed from all remote tracer estimates prior to analysis, that is, $D(\tilde{x}, \tilde{y}) = D_0(\tilde{x}, \tilde{y}) - D_b(\tilde{x})$.

2.3.2. Remotely Derived Shoreline Location and Surf-Zone Boundary

The MASS derived D maps are affected by turbidity, foam and wetted sand. In addition to removing the cross-shore dependent bias $D_b(\tilde{x})$, masks are applied to both land and surf-zone regions. The normalized difference water index ($\mathcal{N}$) is used to separate water pixels from land pixels, where

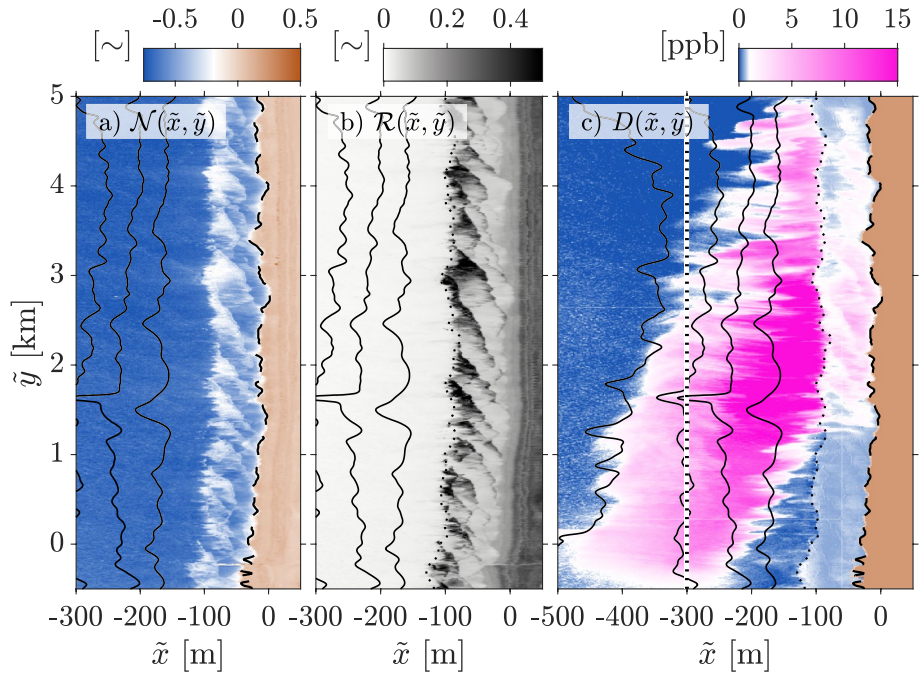

Figure 2. Modular Aerial Sampling System (MASS) derived (a) normalized difference water index $\mathcal{N}$ (3), (b) range-normalized total reflectance $\mathcal{R}$ (4), and (c) near-surface dye concentration D (2) versus transformed cross- and alongshore coordinates $(\tilde{x},\tilde{y})$ at $\mathcal{T} = 6.8$ h. In (a and c) the instantaneous shoreline position ($\mathcal{N} = -0.2$) is indicated with a black dashed line. In (b and c) the offshore edge of active wave breaking ($\mathcal{R} = 0.17$) is denoted with a black dotted line. In (c), the surf-zone dye (between dotted and dashed lines) is shown with 50% transparency and note the different cross-shore domain in (a and b) $-300 \le \tilde{x} \le 50$ m and (c) $-500 \le \tilde{x} \le 50$ m where the thick black/white dashed line denotes $\tilde{x} = -300$ m. Bathymetry contours are drawn at 2 m intervals beginning at 4 m depth.

$$\mathcal{N} = \frac{(\bar{r}(\lambda_{IR}) - \bar{r}(\lambda_G))}{(\bar{r}(\lambda_{IR}) + \bar{r}(\lambda_G))}, \tag{3}$$

uses green band $455 \le \lambda_G \le 485$ nm and near-infrared band $850 \le \lambda_{IR} \le 880$ nm spectral reflectance (e.g., Vos et al., 2019). Land pixels have characteristic $\mathcal{N} > 0$, whereas water pixels typically have $\mathcal{N} < -0.5$ (beige and blue, respectively; Figure 2a). Breaking wave foam has variable $\mathcal{N}$, typically ranging from -0.5 to -0.2 (white streaks, Figure 2a). Here, the land/water threshold is fixed at $\mathcal{N} = -0.2$. The resulting raw instantaneous shoreline is smoothed using a 50 m wide alongshore window and hereafter referred to as the shoreline and denoted $\tilde{x}_{sl}(\tilde{y},\mathcal{T})$ (dashed, Figures 2a and 2c). For visualization purposes in D-maps, regions with $\tilde{x} > \tilde{x}_{sl}$ are colored beige (e.g., Figure 2c).

Surf-zone remote D estimates are strongly affected by breaking wave foam, which can cause false signals as large as 5 ppb and quench true signals by up to 100% (e.g., Clark et al., 2014). For this reason, regions of active wave breaking are identified and remote D is masked before displaying (e.g., Figure 2c). The spectrally integrated radiance (R, 400–990 nm) is adjusted and scaled to form the unity-based normalized total radiance $\mathcal{R}$,

$$\mathcal{R} = \frac{(R - \min\{R\})}{(\max\{R\} - \min\{R\})}, \tag{4}$$

where the maximum and minimum operators are restricted to in-water pixels (where $\mathcal{N} < -0.2$). Surf-zone foam from breaking waves enhances albedo and total reflected radiance (e.g., Frouin et al., 1996; Sinnett & Feddersen, 2016), increasing surf-zone R by roughly a factor of 6 relative to offshore (not shown). As such, the dark streaks in Figure 2b are well defined maxima, whereas these regions have intermediate $\mathcal{N}$ (white streaks) in Figure 2a. Here, a fixed threshold $\mathcal{R} = 0.17$ is used to isolate breaking wave foam, which assuming foam is spectrally white roughly corresponds to an albedo of ≈ 0.12, slightly less than the Sinnett and Feddersen (2016) estimate of mean surf-zone albedo of 0.15. The offshore contour bounding $\mathcal{R} > 0.17$ is smoothed using a 250 m

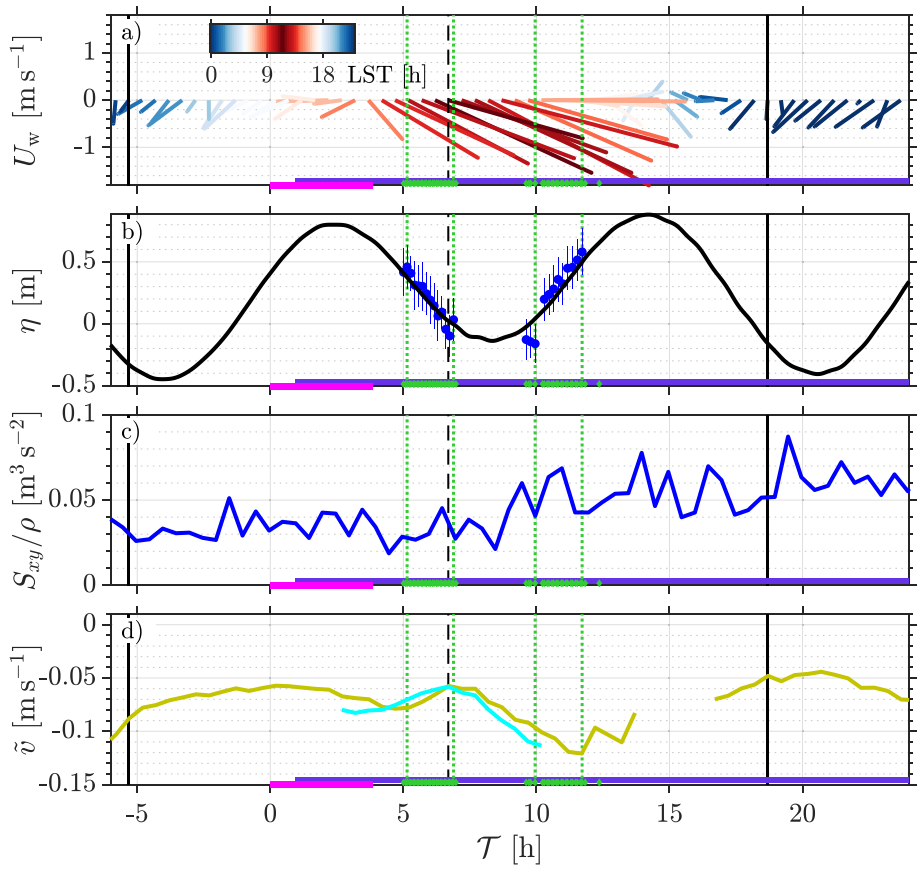

Figure 3. Time-series relative to time since release start $\mathcal{T}$ of (a) wind velocity vectors from the TRNERR MET station, (b) near-shore water-level record η (black) from pressure sensor at WW, (c) off-diagonal component of radiations stress-tensor S_{xy}/ρ (blue) estimated from CDIP buoy, and (d) The depth averaged alongshore currents from locations WW (yellow) and WH (cyan); see Figure 1. In (a) vectors are colored based on the local solar time (LST) in hours. Also in (b) are water-level estimates based on inversion of the $\mathcal{N}$ derived shoreline evolution (5; blue dots) for north-bound flights, with vertical line-segments indicating uncertainty ($\pm \sigma_{sl}/\sqrt{N_{eff}}$). In (c) S_{xy}/ρ is rotated based on the release location shoreline orientation and $S_{xy}/\rho > 0$ indicates northward surf-zone current forcing. In (d) depth-averaged $\bar{v} < 0$ indicates a southward inner-shelf current. Also indicated in (a–d) are mid-night (vertical solid lines) and mid-day (vertical dashed line), the tracer release period (magenta), surf-zone sampling period (purple), and the times of all MASS passes (green, bottom) with green vertical-dotted lines at the times shown in Figure 4.

wide alongshore window to connect individual breaking waves and hereafter referred to as the surf-zone boundary and denoted $\tilde{x}_{sz}(\tilde{y}, \mathcal{T})$ (dotted, Figures 2b and 2c). The surf-zone width is $L_{SZ}(\tilde{y}, \mathcal{T}) = \tilde{x}_{sl} - \tilde{x}_{sz}$, the difference between the shoreline ($\tilde{x}_{sl}$) and surf-zone ($\tilde{x}_{sz}$) boundaries. In the surf-zone, remotely sensed D absolute concentration and spatial gradients (relative concentration) do not necessarily reflect *in situ* surf-zone D variability. To de-emphasize remote D estimates in the surf-zone, pixels between the shoreline and surf-zone boundary are displayed with 50% transparency (e.g., Figure 2c).

3. Experiment Results and Observations

3.1. Experimental Conditions

Experiment winds were typical of a diurnal sea/land-breeze pattern, with early morning offshore-directed speeds of ≈ 2 m s^{-1} becoming onshore-directed with speeds of ≈ 5 m s^{-1} in the afternoon (e.g., Figure 3a). Inner-shelf water level η at WW varied by ≈ 1 m semi-diurnally (black, Figure 3b), and the tracer release (magenta bar) spanned the transition from rising to falling tide. An $\mathcal{N}$-derived water level variation η_{sl} is consistent with observed tidally induced variations (blue, Figure 3b), estimated from the temporal variation in alongshore averaged shoreline position $\bar{x}_{sl}$,

$$\eta_{sl} = \bar{\beta}_{sl}(\bar{x}_{sl} - \bar{x}_{sl,0}), \tag{5}$$

where the over-bar $(\bar{\cdot})$ indicates an alongshore average over > 4 km, and the best fit mean shoreline position and shoreline beach slope are $\bar{x}_{sl,0} = -29$ m and $\bar{\beta}_{sl} = 0.0395$, respectively. Error-bars indicate the uncertainty in η_{sl}, quantified as the ratio, σ_{sl}/N_{dof}, of shoreline alongshore standard-deviation $\sigma_{sl} \approx 10$ m and number of degrees of freedom $N_{dof} = L_y/L_\phi$, with the y-domain length $L_y \approx 9$ km and $\tilde{x}_{sl}$-decorrelation length $L_\phi \approx 1.8$ km. The simple η_{sl} algorithm neglects variations in wave induced swash and setup, but similarity between η and η_{sl} suggest these effects are limited and that the $\mathcal{N}$-derived $\tilde{x}_{sl}$ algorithm is identifying a consistent perceptual land/water interface.

Over $0 \le \mathcal{T} \le 24$ h, the offshore CDIP (Figure 1a) significant wave-height varied weakly $H_s \approx 0.84 \pm 0.05$ m (not shown). Based on the remotely derived shoreline $\tilde{x}_{sl}$ and surf-zone boundary $\tilde{x}_{sz}$, the time- and alongshore-averaged surf-zone width $\bar{L}_{SZ} = 77.3 \pm 2.3$ m, was relatively constant in time, with ⋮-averaged t-standard deviation of 2.25 m. The t-averaged ⋮-standard deviation of L_{SZ} was $\sigma_{sz} = 12$ m, implying that wave breaking was predominately confined to $\tilde{x} > -(\bar{L}_{SZ} + 2\sigma_{sz}) \approx 100$ m, and hereafter $L_{SZ} = 100$ m is used for the surf-zone width. The off-diagonal component of the radiation stress tensor S_{xy}/ρ, oriented to the shoreline angle at the release, was relatively constant early $0 \le \mathcal{T} \le 8$ h (Figure 3c), but later increased by a factor of ≈ 2 due to steepening of the incident wave angle (not shown). Positive S_{xy}/ρ corresponds to waves incident from a southerly direction (south-swell) forcing positive-⋮ surf-zone currents. In contrast, the inner-shelf depth-averaged alongshore currents at WW and WH were negative (southward, Figure 3d), varying between ≈ 0.05 and 0.10 m s^{-1}. Thus indicating cross-shore shear in the alongshore currents and implying differential surf-zone and inner-shelf alongshore tracer transport.

3.2. Surf-Zone and Inner-Shelf Descriptive Tracer Evolution

The overall observed tracer evolution is first described qualitatively using the remotely sensed (i.e., MASS) D (Figure 4), and *in situ* inner-shelf alongshore D and T transects (Figure 5) and surf-zone D time-series (Figure 6). When remote sampling began, at $\mathcal{T} = 5$ h, the surf-zone released tracer had already spread offshore to $\tilde{x} \approx -800$ m near the release and spanned roughly 4 km alongshore within the surf-zone (Figure 4a). At this time, surf-zone tracer is entirely north of the release location owing to northward surf-zone transport $S_{xy}/\rho > 0$ (Figure 3c).

In the region $\tilde{y} < 2$ km for $5 < \mathcal{T} < 7$ h, the inner-shelf plume narrowed in the cross-shore by up to ≈ 300 m. Grimes, Feddersen, Giddings, and Pawlak (2020) determined the deformation was advection dominated by the local internal tide (IT) circulation, and was largely balanced by deepening of inner-shelf tracer. The IT cooling phase cross-shore exchange flow advected tracer offshore near-surface early, and then reversed around $\mathcal{T} = 5$ h causing the observed deformation. Southward inner-shelf transport also increased in the afternoon (not shown), consistent with the observed increase in depth averaged alongshore current at WH (cyan, Figures 3d and 4a–4c). Here, focus is restricted to the surf-zone/inner-shelf evolution predominately north of $\tilde{y} = 2$ km.

For $\mathcal{T} > 5$ h, tracer was transported to the north in the surf-zone ($\tilde{y} \gtrapprox 2$ km) and to the south on the inner-shelf ($\tilde{y} < 2$ km). The MASS derived northward plume progression was relatively steady. Note, there may a be time-lag between the arrival of surf-zone tracer at ⋮ and the development of inner-shelf MASS D-signal, owing to cross-shore exchange time-scales. Northward progression is tracked using the northern inner-shelf plume front $\tilde{y}_f(\mathcal{T})$ (red ×'s, Figures 4a–4d), defined as the northern-most instance of, $D^{is}(\tilde{y}, \mathcal{T}) \ge \max\left\{D^{is}\right\}_{(\tilde{y})}/20$, where $D^{is}(\tilde{y}, \mathcal{T})$ is the $\tilde{x}_{sz} - 75$ m $\le \tilde{x} \le \tilde{x}_{sz}$ cross-shore averaged remotely sensed $D(\tilde{x}, \tilde{y}, \mathcal{T})$ and $\max\{\cdot\}_{(\tilde{y})}$ is the ⋮-direction maximum operator. As time increases from $\mathcal{T} = 5.1$ to 11.7 hr, $\max\left\{D^{is}\right\}_{(\tilde{y})}$ decreases from 21 to 4 ppb, hence the decreasing color-ranges used in Figures 4a–4d which can cause perceptive differences in the dye-signal at $\tilde{y}_f$. The cross-shore averaged D^{is} has a minimum signal detection level of ∼0.1 ppb, such that, when $\max\left\{D^{is}\right\}_{(\tilde{y})} = 4$ ppb the front position threshold $\max\left\{D^{is}\right\}_{(\tilde{y})}/20 \ge 0.2$ ppb is detectable.

At all times, inner-shelf remotely sensed D within 1.5 km of the northward-propagating front $\tilde{y}_f$ is confined to $\tilde{x} > -400$ m (Figure 4). The cross-shore widening with distance away from the northward propagating front $\tilde{y}_f$ is indicative of cross-shore exchange. The alongshore variation of inner-shelf remotely sensed D, resembling billows, is indicative of rip-current ejections of dye-laden surf-zone water (e.g., Hally-Rosendahl et al., 2015).

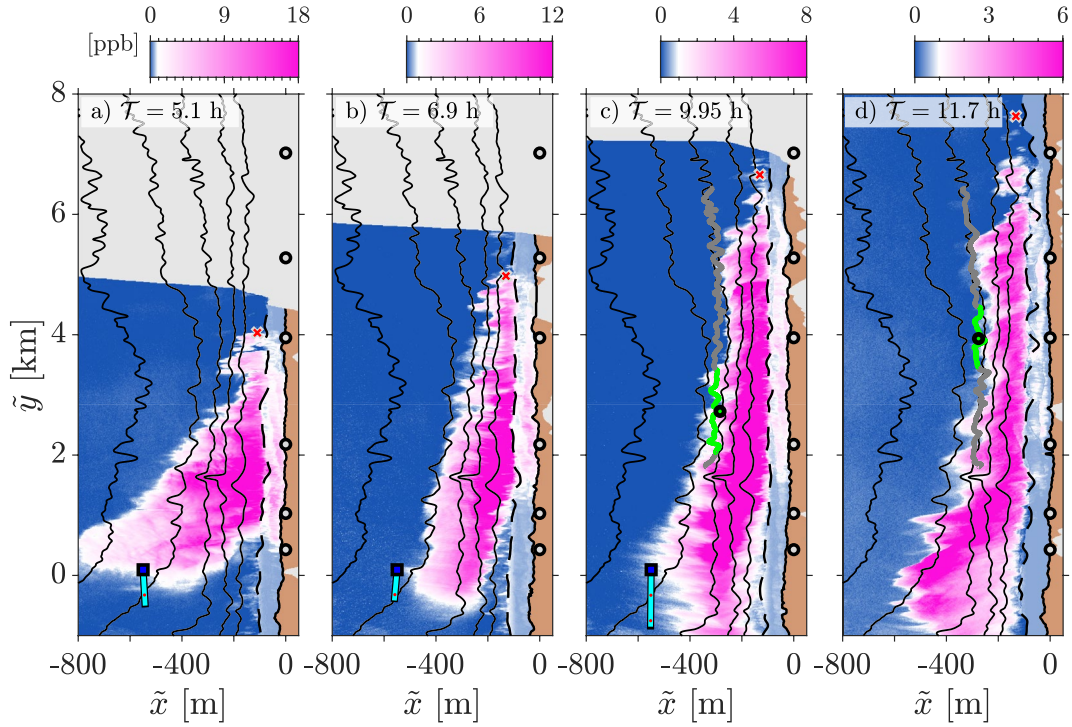

Figure 4. (a–d) Surface dye concentration D vs. quasi-shorenormal coordinates $(\tilde{x}, \tilde{y})$ for (a) $\mathcal{T} = 5.1$ h, (b) $\mathcal{T} = 6.9$ h, (c) $\mathcal{T} = 9.95$ h, and (d) $\mathcal{T} = 11.7$ h, corresponding to the green vertical-dotted lines in Figure 3. The MASS estimated northern inner-shelf plume front position $\tilde{y}_f$ (red ×'s). Note the D color scales decrease with $\mathcal{T}$, with blue-to-magenta color transition at (a–c) $D = 1$ ppb and (d) $D = 0.5$ ppb. In (a–c) the depth-averaged alongshore current (cyan) is indicated at WH (blue) with 5 cm s^{-1} increments indicated by a red dot. In (c and d) inner-shelf alongshore north-bound (c) and south-bound (d) transects are shown in gray with the current vessel position (black circle) and ±10 min highlighted in light green. Regions without data are gray, the region between the break-point and shoreline ($\tilde{x}_{sz} \le \tilde{x} \le \tilde{x}_{sl}$) is semi-transparent, and the region onshore of the shoreline ($\tilde{x} > \tilde{x}_{sl}$) is brown. Bathymetry contours drawn at 2 m intervals for $h \ge 4$ m.

Inner-shelf *in situ* D was observed mid-to late-afternoon ($9.7 < \mathcal{T} < 12.5$ h) along the two alongshore transects (Figures 4c, 4d, 5a and b), spanning 1.2–1.5 hr each. At $\mathcal{T} = 9.95$ h, the vessel was northbound and located at $\tilde{x} \approx -285$ m and $\tilde{y} \approx 2.7$ km, roughly corresponding to the black circle in Figure 4c and black circle at the top of Figure 5a. During both northbound and southbound inner-shelf transects, D is alongshore patchy and predominately surface concentrated ($z > -4$ m), with decreasing occurrence and intensity with increasing $\tilde{y}$. Regions with $D \ge 1$ ppb generally coincide with vertical bands of warmer temperature fluid (Figures 5c and 5d). The D and T covariation results from the mid-to late-afternoon surf-zone being warmer than the inner-shelf due to strong solar heating (e.g., Grimes, Feddersen, Giddings, & Pawlak, 2020; Hally-Rosendahl et al., 2014). As *in situ* tracer is near-surface concentrated (Figures 5a and 5b), remotely sensed D inner-shelf patterns are considered representative of the horizontal tracer distribution, although absolute concentrations differ from the alongshore transect because remotely sensed D estimates are sensitive to D vertical structure and optical depth (which are not considered here). Considered jointly, the remote surface and *in situ* sub-surface D suggest the majority of tracer over $\tilde{y} > 2$ km is confined to $\tilde{x} > -300$ m up to ≈ 12 h after the start of tracer release.

As surf-zone breaking wave foam masks remote D signal, surf-zone D evolution is analyzed using fixed instruments distributed alongshore between $\tilde{y} = 0.4$ and 6.9 km (gray dots, Figure 4), and averaged over 30 min to remove variability due to combination of very low-frequency currents and spatial tracer gradients. Near the tracer release, at $\tilde{y} = 0.4$ km, tracer signal arrived prior to instrument deployment (Figure 6a). For $\mathcal{T} < 4.5$ h, D was on average 65 ppb with a temporal maximum $D_{max} = \max\{D\}_{(t)} = 90$ ppb (teal diamond) and significant (≈±62 ppb) temporal variability (gray shading). The large variability of 30-min D indicates that surf-zone horizontal tracer gradients were large at $\tilde{y} = 0.4$ km, and we refer to this region as the near-field similar to Brown et al. (2019). Just before $\mathcal{T} = 5$ h, the tracer signal rapidly decays, and we define the time of surf-zone plume passage $\mathcal{T}_p$ (red ▽) as the latest instance of $D(\mathcal{T}) \ge (1 + D_{max}/4)$, where the additional 1 ppb compensates for

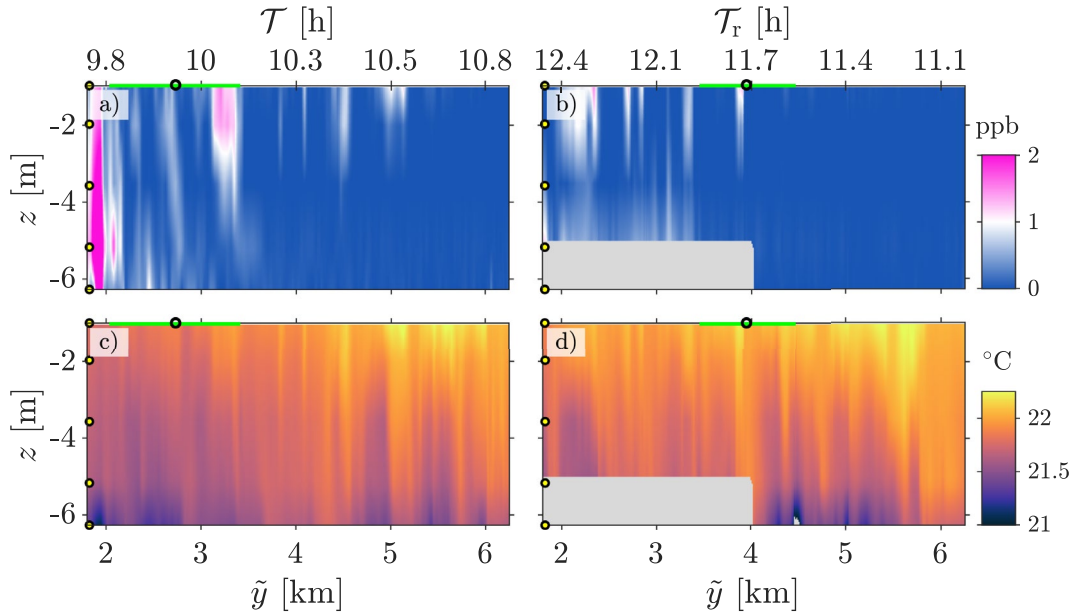

Figure 5. Inner-shelf alongshore transects of (a and b) dye concentration D and (c and d) temperature T versus alongshore coordinate $\tilde{y}$ (bottom) or time since release start $\mathcal{T}$ (top) and vertical z. Left panels (a and c) correspond to the north-bound transect (Figure 4c); right panels (b and d) correspond to the south-bound transect (Figure 4d). The yellow markers (left) indicate instrument depths and the green bar (top) indicates the vessel position (±10 min) for D panels in Figures 4c and 4d. Note in (b and d) $\mathcal{T}$ increases right-to-left due to the vessel trajectory. Gray regions indicate missing data.

the surf-zone fluorometer minimum detection level and the higher *in situ* $D_{max}/4$ threshold buffers for increased temporal variability. Results are not sensitive to the choice of remote and *in situ* threshold. After $\mathcal{T} = 5$ h, the D-signal falls below the minimum detection level and does not rise again, indicating that tracer advected offshore of this location by the IT (Grimes, Feddersen, Giddings, & Pawlak, 2020) early was not re-entrained into the surf-zone at measurable levels subsequent to the cross-shore deformation (Figures 4b–4d).

At $\tilde{y} = 1$ km, D-signal increases at about $\mathcal{T} = 1$ h, and the time of surf-zone plume front arrival ($\mathcal{T}_f$; green x, Figure 6b) is taken as the first instance of $D(\mathcal{T}) \geq (1 + D_{max}/4)$, analogous to $\mathcal{T}_p$. Here, D variability is weaker (≈±18 ppb) relative to the maximum $D_{max} = 55$ ppb (teal diamond, Figure 6b), indicating weaker surf-zone D gradients and $\tilde{y} > 1$ km is termed the far-field. The D-signal time of passage $\mathcal{T}_p$ occurred some time during the low-tide data gap, before $\mathcal{T} = 7.5$ h, and did not return at levels significantly above the minimum detection level (purple dashed line, Figure 6b). At increasing $\tilde{y}$, the pattern of later front arrival $\mathcal{T}_f$ (green △'s) and decreasing D_{max} (teal diamonds) continues, and D-signal temporal width $\mathcal{W} = \mathcal{T}_p - \mathcal{T}_f$ increases (separation of red/green *symbols*, Figure 6f). The shape of D time-series also evolve downstream: for $\tilde{y} < 2$ km, $D(\mathcal{T})$ resembles a top-hat, rapidly increasing and later rapidly decaying, whereas for $\tilde{y} > 2$ km the signals become skewed, rapidly increasing and slowly tapering off.

3.3. Quantitative Tracer Evolution

Surf-zone alongshore tracer transport, dilution, and spreading are quantified using defining features from the observed plume evolution. First, an alongshore tracer transport speed v_{SZ} is estimated from the remotely derived northward plume front $\tilde{y}_f$ progression (red ×'s, Figure 4), and the surf-zone D front arrival time $\mathcal{T}_f$ (green △'s, Figure 6). The best fit constant speed derived from $\tilde{y}_f$ is 0.185 m s^{-1} (red dashed, Figure 7a) and derived from $\mathcal{T}_f$ is 0.182 m s^{-1} (green dashed), giving a mean $v_{SZ} = 0.183$ m s^{-1} (solid black). The plume progression based v_{SZ} estimate assumes that alongshore transport is advection dominated (i.e., moderate Péclet number). A model for wave-driven surf-zone advective speed (v_{SZ}^{mod}) based on alongshore wave forcing balanced by linear drag is estimated as,

$$v_{SZ}^{mod} \approx S_{xy}/(\rho L_{SZ} \mu), \tag{6}$$

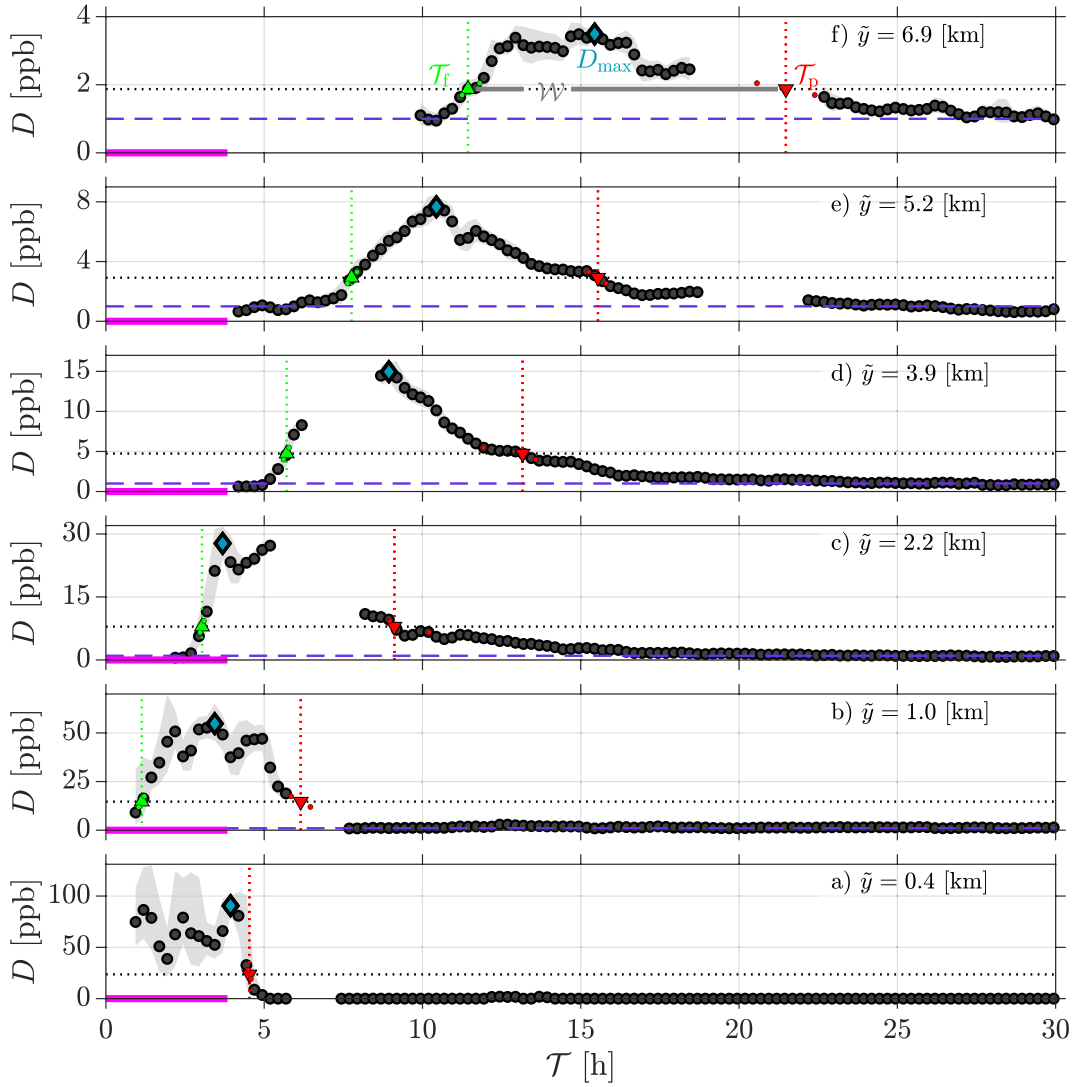

Figure 6. (a–f) Surf-zone (30-min averaged) dye concentration D (black circles), with the corresponding standard deviation (gray shading) versus time since start of tracer release $\mathcal{T}$ and alongshore $\tilde{y}$ increasing bottom to top as indicated in each panel. Also indicated are the maximum concentration D_{max} (teal diamond), the surf-zone plume concentration threshold (horizontal dotted line) and corresponding arrival time $\mathcal{T}_f$ (green $\triangle$'s and vertical dotted lines) and passage $\mathcal{T}_p$ (red $\triangledown$'s and vertical dotted lines) and assuming $\pm 5\%$ change in threshold (colored dots), and the surf-zone fluorometer minimum detection level $D = 1$ ppb (dashed purple).

where the radiation stress divergence occurs uniformly over the surf-zone width L_{SZ}, and μ [m s^{-1}] is a dimensional Rayleigh friction coefficient (e.g., Feddersen et al., 2000; Lentz et al., 1999). Least-squares fit between the observed mean tracer alongshore transport speed $v_{SZ} \approx 0.18$ m s^{-1} and the offshore S_{xy} observed over $0 \leq \mathcal{T} \leq 12$ h results in best fit coefficient $\mu = 0.197/L_{SZ} \approx 2.5 \times 10^{-3}$ m s^{-1}, implying a surf-zone frictional time-scale of O(10 min) consistent with previous observations (Feddersen et al., 2000; Lentz et al., 1999). Time integrating Equation 6 gives a wave estimated northern plume front position $\tilde{y}_f^{mod}$ that largely tracks the observed arrivals over $\mathcal{T} \approx 10$ h and $\tilde{y} \approx 6$ km (blue, Figure 7a). Thus, classic surf-zone alongshore momentum dynamics are applicable and effects of shoreline curvature are negligible over the scales considered herein.

Exchange with the inner-shelf and alongshore mixing cause downstream decay in maximum concentration D_{max} (Figures 6f and 7b), with D_{max} decreasing from roughly 90 ppb near the release to < 5 ppb at $\tilde{y} = 7$ km. The associated e-folding length scale is roughly 1.6 km, and moving at constant speed v_{SZ} corresponds to a time-scale ≈ 2.5 h. Similar to the maximum concentration, the 30-min standard deviation at D_{max} also decreases strongly with distance (error bars, Figure 7b). As the surf-zone observations have gaps, the tracer mass advected past

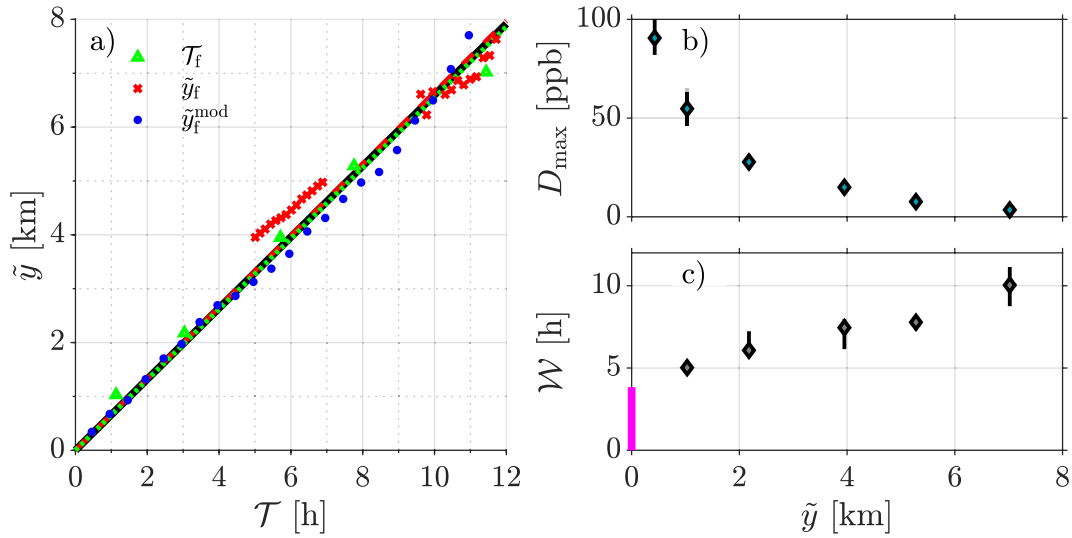

Figure 7. (a) Alongshore ( ) northern plume front location versus time since release start $\mathcal{T}$ based on the surf-zone plume front arrival time $\mathcal{T}_f$ (green △'s; see also Figure 6), the northern inner-shelf plume front position $\tilde{y}_f$ (red ×'s), and estimated from observed wave forcing $\tilde{y}_f^{mod}$ (blue dots). The green and red dashed lines are regressions using associated dots and forced through the origin; the black solid line is the average $v_{SZ} \approx 0.18$ m s^{-1}. (b) Maximum observed surf-zone dye concentration D_{max} (teal diamonds) with the corresponding 30-min standard deviation (error bars). (c) Tracer signal temporal width $\mathcal{W}$ (gray diamonds) defined as the time-difference between the up/down (red/green) triangles in Figure 6 and assuming ±5% change in threshold (error bars).

each instrument cannot be determined. Instead, the D-signal temporal width, denoted $\mathcal{W} = \mathcal{T}_p - \mathcal{T}_f$ (Figures 6f and 7c), is used as a characteristic time-scale. At $\tilde{y} = 0$, the release duration is assumed for the initial temporal width $\mathcal{W}_0 = 3.84$ h (magenta, Figure 7c). As distance/time from release increases, the width $\mathcal{W}$ increases roughly linearly, where the error bars indicate the effect of modifying the thresholds in $\mathcal{T}_f$ and $\mathcal{T}_p$ by ±5%. Assuming a scale estimate for the time-integral of D proportional to ($D_{max}\mathcal{W}$), the observed $\mathcal{W}$ linear increase with and D_{max} exponential decay imply that overall the tracer mass advected past a stationary observer decays exponentially downstream. Thus, exchange between the surf-zone and inner-shelf significantly decreases downstream surf-zone tracer mass, that is, decreasing water quality impacts associated with point source pollution events.

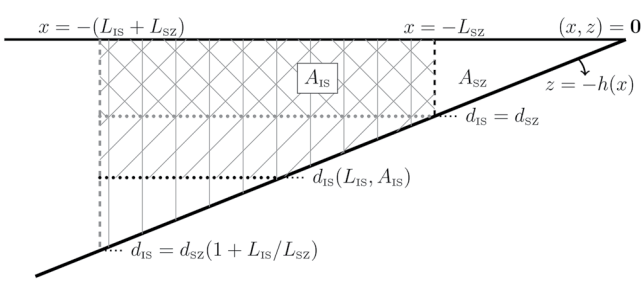

Figure 8. Diagram of surf-zone/inner-shelf box model parameters: surf-zone cross-sectional area A_{SZ} onshore of $x = -L_{SZ}$ (black dashed), assuming constant beach slope d_{SZ}/L_{SZ}, and the inner-shelf area A_{IS} over $-(L_{IS} + L_{SZ}) \le \tilde{x} < -L_{SZ}$ for three different effective inner-shelf dye depths d_{IS}, illustrating a vertically well mixed inner-shelf $d_{IS} = d_{SZ}(1 + L_{IS}/L_{SZ})$ (vertical lines), stratified surface plume $d_{IS} = d_{SZ}$ (northwest lines above dotted gray), and an arbitrary intermediate value $d_{IS} = 1.8\ d_{SZ}$ (northeast lines above dotted black) which depends on L_{IS} and A_{IS}.

4. Coupled Surf-Zone/Inner-Shelf Tracer Modeling

The observed large-scale surf-zone tracer evolution is simulated and connected to underlying dynamics and physical mechanisms using a coupled surf-zone/inner-shelf box tracer model, analogous to fast/slow-zone decompositions applied to open channel flows (Chatwin, 1971; Chikwendu & Ojiakor, 1985; Elder, 1959). The model surf-zone depth and cross-shore averaged tracer concentration $D_{SZ}(\tilde{y}, t)$ is defined as,

$$D_{SZ}(\tilde{y}, t) = A_{SZ}^{-1} \int_{-L_{SZ}}^{0} \int_{-h(\tilde{x})}^{0} \langle D(\tilde{x}, z, \tilde{y}, t) \rangle \, \mathrm{d}z \, \mathrm{d}\tilde{x} \tag{7}$$

where $\langle \cdot \rangle$ represents a Reynolds (time) average, and the surf-zone cross-sectional area is $A_{SZ} = d_{SZ}L_{SZ}/2$, assuming a surf-zone width $L_{SZ} = 100$ m, surf-zone depth $d_{SZ} = 2$ m and planar bathymetry $h(\tilde{x}) = -\tilde{x}\, d_{SZ}/L_{SZ}$ (Figure 8). Model inner-shelf cross-sectional area-averaged tracer concentration (D_{IS}) is similarly defined as,

$$D_{IS}(\tilde{y}, t) = A_{IS}^{-1} \int_{-(L_{IS}+L_{SZ})}^{-L_{SZ}} \int_{-\min\{h, d_{IS}\}}^{0} \langle D(\tilde{x}, z, \tilde{y}, t) \rangle \, \mathrm{d}z \, \mathrm{d} \tag{8}$$

where L_{IS} and d_{IS} define the geometry of the box model inner-shelf area A_{IS} (Figure 8), from which tracer can readily re-entrain into the surf-zone. In this way, the inner-shelf is subdivided into a narrow region A_{IS} that affects surf-zone tracer evolution and an outer inner-shelf region (offshore of $x = -(L_{SZ} + L_{IS})$ and below $z = -d_{IS}$) that does not affect surf-zone tracer evolution on time-scales < 30 h. Hereafter, inner-shelf denotes the box model region A_{IS}, unless otherwise noted.

The inner-shelf cross-shore length-scale L_{IS} is expected to depend on rip-current cross-shore extent, and is estimated to be $50 \le L_{IS} < 200$ m based on the remotely sensed surface D within ≈ 2 km of $\tilde{y}_f$ (red ×, Figure 4). Variable inner-shelf dye depth d_{IS} in Equation 8 accounts for varying inner-shelf stratification, and its effect on the inner-shelf area A_{IS}. If the inner-shelf is vertically well mixed, such that $d_{IS} = d_{SZ}(1 + L_{IS}/L_{SZ})$, then $A_{IS} = L_{IS}d_{SZ}(1 + L_{IS}/(2L_{SZ}))$ (vertical gray lines, Figure 8). If the inner-shelf is stratified, with a well mixed surface dye layer of depth $d_{IS} = d_{SZ}$ and dye free lower layer, then $A_{IS} = L_{IS}d_{SZ}$ (above the dotted gray, Figure 8). The afternoon observed near-surface intensified inner-shelf D suggests $d_{IS} \approx 4$ m (Figures 5a and 5b). Alternate inner-shelf plume configurations are possible but not considered herein, for example, sub-surface or near bottom inner-shelf plume could result from dense surf-zone fluid relative to the adjoining inner-shelf. Parameters L_{IS} and A_{IS} will be estimated by optimizing an idealized tracer model simulation of surf-zone observations.

To model dye evolution at the observed scales, the following tracer equations are used:

$$\frac{\partial D_{SZ}}{\partial t} + v_{SZ}\frac{\partial D_{SZ}}{\partial \tilde{y}} = \underbrace{-k_{SZ}(D_{SZ} - D_{IS})}_{\text{SZ/IS Exch.}} + \underbrace{K_{\tilde{y}\tilde{y}}\frac{\partial^2 D_{SZ}}{\partial \tilde{y}^2}}_{\text{SZ Shear-Disp.}} + \underbrace{Q_0\delta(\tilde{y})\Pi(\mathcal{T})}_{\text{Dye Rlse.}}, \tag{9}$$

$$\frac{\partial D_{IS}}{\partial t} + v_{IS}\frac{\partial D_{IS}}{\partial \tilde{y}} = \underbrace{\gamma k_{SZ}(D_{SZ} - D_{IS})}_{SZ/IS\ \ Exch.} - \underbrace{k_{IS}D_{IS}}_{\text{IS Loss}}, \tag{10}$$

where $v_{SZ} = 0.18$ m s^{-1} and $v_{IS} = 0.05$ m s^{-1} are constant surf-zone and inner-shelf area-averaged alongshore velocities. Consistency between v_{SZ} based on northward tracer transport and the radiation-stress based formulation v_{SZ}^{mod} suggests an empirical v_{SZ} formulation may also be used. The v_{IS} estimate is the cross-sectional area average between v_{SZ} at $x = -100$ m and the ≈ 12 m WH alongshore velocity (≈ -0.08 m s^{-1}, Figures 3d and 4a–4c), assuming the depth-averaged current varies linearly cross-shore. The tracer release is modeled as a delta-function, $\delta(\tilde{y})$, at $\tilde{y} = 0$ and top-hat in time, that is, $\Pi(\mathcal{T}) = 1$ for $0 < \mathcal{T} \le \mathcal{W}_0$, and $\Pi(\mathcal{T}) = 0$, otherwise. The constant source rate $Q_0 = M/(A_{SZ}\Delta\tilde{y}\mathcal{W}_0)$ [ppb s^{-1}] uniformly distributes the experiment total dye mass M [ppb m^3] over the discrete surf-zone volume ($A_{SZ}\Delta\tilde{y}$), with alongshore resolution $\Delta\tilde{y} = 16$ m ($< L_{SZ}/4$), and over the release duration $\mathcal{W}_0 = 3.84$ h.

The first right hand side (RHS) term of Equation 9 and 10 parameterizes surf-zone/inner-shelf tracer exchange (at $\tilde{x} = -L_{SZ}$), for example, due to rip-currents, through a surf-zone exchange rate k_{SZ} by assuming the depth-integrated tracer flux depends on the difference in mean concentrations multiplied by an exchange velocity (e.g., Hally-Rosendahl et al., 2015),

$$A_{SZ}^{-1}u_{EX}d_{SZ}(D_{SZ} - D_{IS}) \approx A_{SZ}^{-1}\int_{-d_{SZ}}^{0}\langle u(z,t)D(z,t)\rangle\,\mathrm{d}z, \tag{11}$$

where the integrand represents the Reynolds averaged advective tracer flux, and exchange velocity u_{EX} quantifies the rip-current statistics (e.g., Boehm, 2003). The factor $\gamma = A_{SZ}/A_{IS}$ in Equation 10 accounts for the difference in cross-sectional area. The resulting surf-zone exchange rate k_{SZ} has the form,

$$k_{SZ} \propto u_{EX}/L_{SZ}, \tag{12}$$

and based on a previous field surf-zone/inner-shelf tracer experiment in similar conditions u_{EX} is anticipated to be $\mathcal{O}(1$ cm s$^{-1})$ (Hally-Rosendahl et al., 2015), giving $k_{SZ} \sim 10^{-4}$ s^{-1}.

Using similar arguments, the last term of Equation 10 uses an inner-shelf exchange rate k_{IS} to parameterize tracer losses at $\tilde{x} = -(L_{IS} + L_{SZ})$ (vertical dashed gray line, Figure 8) and through vertical mixing at $z = -d_{IS}$ (dotted horizontal lines, Figure 8). Assuming a vertically well-mixed inner-shelf area (vertical solid lines, Figure 8), k_{IS} is also proportional to an exchange velocity and inverse length-scale (i.e., L_{IS}^{-1}). As rip-current induced cross-shore

exchange potential decreases with distance offshore of the surf-zone (e.g., Suanda & Feddersen, 2015), it is anticipated that $k_{IS} < k_{SZ}$, however other inner-shelf processes like nonlinear internal waves and baroclinic exchange flows can contribute to k_{IS}.

The second RHS term in Equation 9 represents surf-zone shear dispersion, accounting for covariance between the perturbation tracer concentration $D'(\tilde{x}, z, \tilde{y}, t) = D - D_{SZ}$ and sheared alongshore velocity $v'(\tilde{x}, z, \tilde{y}, t) = v - v_{SZ}$,

$$K_{\tilde{y}\tilde{y}} \frac{\partial^2 D_{SZ}}{\partial \tilde{y}^2} \approx A_{SZ}^{-1} \frac{\partial}{\partial \tilde{y}} \left[\int_{-L_{SZ}}^{0} \int_{-h(\tilde{x})}^{0} \langle v'(x,z,t) D'(x,z,t) \rangle \, \mathrm{d}z \, \mathrm{d}x \right]. \tag{13}$$

where the approximation assumes the observed v_{SZ} is constant and well represented, v' statistics are stationary, and that both are alongshore uniform. Thus, the LHS of Equation 13 is analogous to the asymptotic behavior of tracers in channel and pipe flow (Spydell & Feddersen, 2012a; Taylor, 1954). Surf-zone shear dispersion is generally scaled as $K_{\tilde{y}\tilde{y}} \sim v_{SZ}^2 L_{SZ}^2 / K_{\tilde{x}\tilde{x}}$ (Spydell & Feddersen, 2012b; Spydell et al., 2009) based on the cross-shore diffusivity $K_{\tilde{x}\tilde{x}}$ induced by horizontal eddies (vertical vorticity, e.g., Clark et al., 2010). A constant surf-zone shear dispersion coefficient $K_{\tilde{y}\tilde{y}} = 5 \ \mathrm{m^2\,s^{-1}}$ is used, based on ≤1 hr surf-zone drifter releases in similar surf-zone alongshore currents $O(15 \ \mathrm{cm\,s^{-1}})$ (e.g., Spydell et al., 2009), implying a relatively short Lagrangian (diffusive) time-scale of $K_{\tilde{y}\tilde{y}} / v_{SZ}^2 \approx 2.5$ min (Spydell & Feddersen, 2012b).

The coupled surf-zone/inner-shelf tracer model Equations 9 and 10 is solved numerically on a discrete alongshore domain $-4 < \tilde{y} < 8$ km with $\Delta\tilde{y} = 16$ m resolution. Equations were discretized using a second-order accurate flux-limiting upwind difference scheme for advection terms (Roe, 1986), a second-order accurate centered difference scheme for the diffusive term, and time-stepped using a first-order scheme. A time step of $\Delta t = 12$ s was used, well below the Courant ($v_{SZ}\Delta t / \Delta\tilde{y} \le 1$) and Fourier ($K_{\tilde{y}\tilde{y}}\Delta t / \Delta\tilde{y}^2 \le 1/2$) stability criteria. Diffusive and dispersive numerical errors can affect propagating signals in regions of large alongshore tracer gradients (i.e., near the release) and generally increase with the size of $\Delta\tilde{y}$ and Δt. However, scale estimates for the numerical diffusion coefficient in surf-zone is negligible relative to $K_{\tilde{y}\tilde{y}}$ and is $< 0.5 \ \mathrm{m^2\,s^{-1}}$ on the inner-shelf. Moreover, results are not sensitive to $\Delta\tilde{y}$ variations between 10 and 80 m or using either a first-order or second-order upwind-biased numerical advection scheme.

There are 6 model parameters, $\{v_{SZ}, v_{IS}, K_{\tilde{y}\tilde{y}}, k_{SZ}, k_{IS}, \gamma\}$, and $\{v_{SZ}, v_{IS}, K_{\tilde{y}\tilde{y}}\}$ were estimated from the observations and held constant. The remaining three parameters $\{k_{SZ}, k_{IS}, \gamma\}$ were optimized via iterative search to minimize the signal-variance normalized squared-error ε between the observed D and modeled D_{SZ},

$$\varepsilon = \sum_{\tilde{y}} \overline{(D - D_{SZ})^2}^{(t)} \sigma_D^{-2}, \tag{14}$$

with signal variance,

$$\sigma_D^2(\tilde{y}) = \overline{D^2}^{(t)},$$

where $\bar{(\cdot)}^{(t)}$ indicates the time average. The surf-zone/inner-shelf exchange rate k_{SZ} was varied by a factor of 2 from 7×10^{-5} to 1.5×10^{-4} s^{-1} at 1×10^{-5} s^{-1} intervals, whereas the inner-shelf exchange rate k_{IS} was varied between 2×10^{-5} and 9×10^{-5} s^{-1}. To determine A_{IS}, the ratio of surf-zone to inner-shelf area γ was varied between 0.125 and 0.8 by varying L_{IS} in increments of $0.125 L_{SZ}$ using the vertically well mixed formalism (vertical gray lines, Figure 8). Using the stratified definition of d_{IS} as an upper bound on L_{IS}, the optimal $A_{IS} = A_{SZ}/\gamma$ implies $L_{IS} \le A_{SZ}/(\gamma d_{SZ})$ (north west sloping lines, Figure 8). At each iteration of $\{k_{SZ}, k_{IS}, \gamma\}$, the model solution D_{SZ} was interpolated to the far-field observations ($\tilde{y} > 1$ km, Figures 6c–6f). Estimate of $\varepsilon(k_{SZ}, k_{IS}, \gamma)$ was restricted to $D > 1.5$ ppb and times $(\mathcal{T} - \tilde{y}/v_{SZ}) \le 15$ h, limiting the influence of surf-zone turbidity spikes on errors.

The resulting set of parameters with minimum $\varepsilon \approx 0.1$, or standard-error $(\sigma_D \varepsilon) \approx 1$ ppb, are,

$$k_{SZ} = (1.2 \pm 0.3) \times 10^{-4} \ [\mathrm{s^{-1}}]$$
$$k_{IS} = (5.0 \pm 2.8) \times 10^{-5} \ [\mathrm{s^{-1}}]$$
$$\gamma = 0.33 \pm 0.09,$$

where uncertainties are based on the estimated curvature of $\varepsilon(k_{SZ}, k_{IS}, \gamma)$, for example, $(\partial^2 \varepsilon / \partial k_{SZ}^2)^{-1/2} = 0.3 \times 10^{-4}$ s^{-1}, etc. There were no other (local) minima within the parameter ranges. The optimized model D_{SZ} curves (solid red,

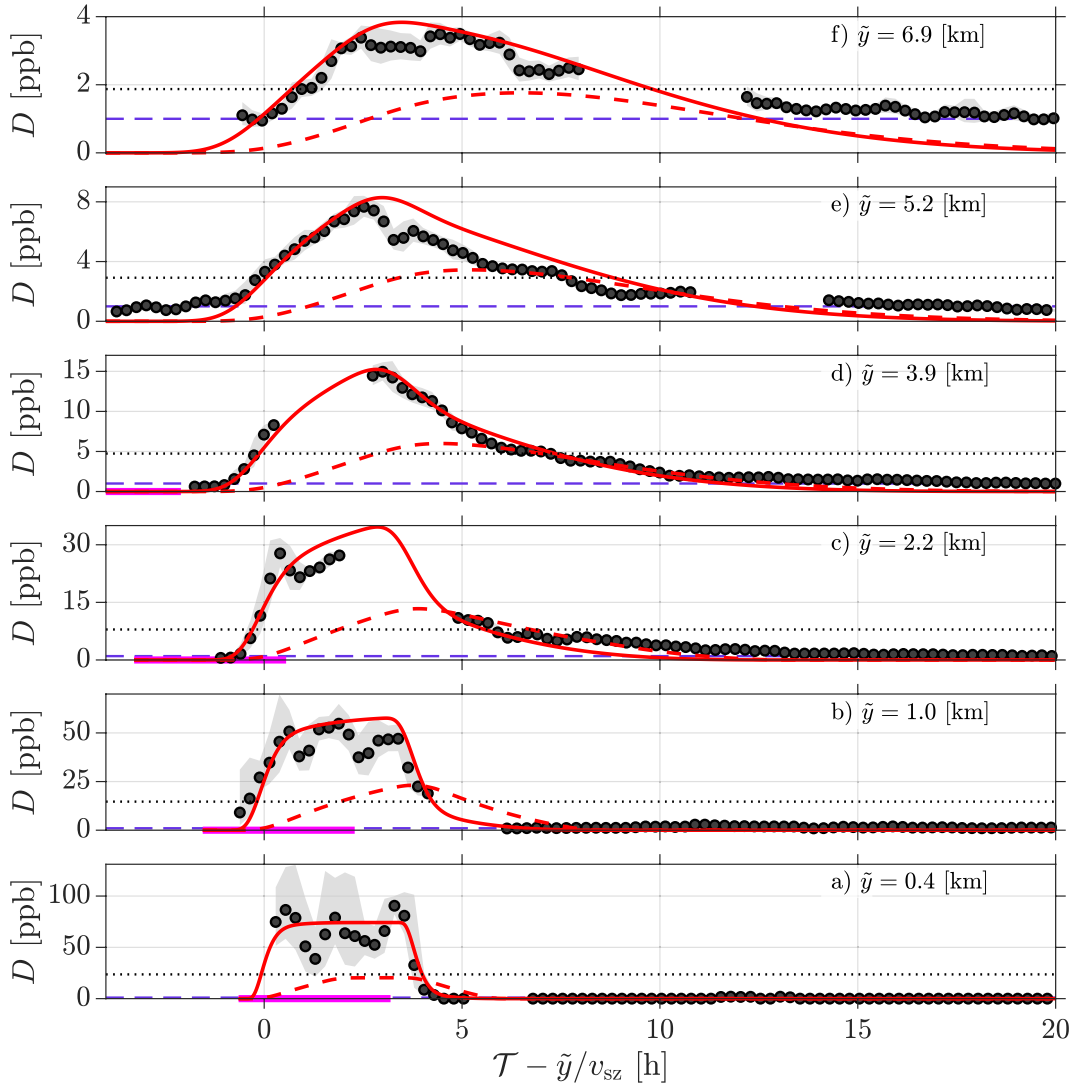

Figure 9. (a–f) Surf-zone dye concentration D from observations (black circles, gray shading; see Figure 6) and D_{SZ} (solid red curves) modeled using optimal parameters, versus shifted time ($\mathcal{T} - \tilde{y}/v_{SZ}$) and alongshore $\tilde{y}$ (increasing bottom to top as indicated in each panel). Modeled inner-shelf concentration D_{IS} (dashed red) is shown at each instrument location. Also indicated is the surf-zone plume concentration threshold (dotted black) and surf-zone fluorometer minimum detection level $D = 1$ ppb (dashed purple).

Figure 9) generally reproduce the observed surf-zone D time-series up to $\tilde{y} \approx 7$ km. Time-series are displayed using a shifted time coordinate ($\mathcal{T} - \tilde{y}/v_{SZ}$), based on the estimated plume arrival time ($\tilde{y}/v_{SZ}$).

In the near-field, $\tilde{y} \leq 1$ km, both observed D and modeled D_{SZ} decay prior to roughly ($\mathcal{T} - \tilde{y}/v_{SZ}$) = 5 h and remain low following the plume passage (Figure 9a). The model curves are smooth as D_{SZ} represents Reynolds averaged (time-averaged) bin-mean tracer evolution. At $\tilde{y} = 1$ km, both also resemble an approximate top-hat (Figure 9b), rapidly increasing then leveling for ~2 hr before decaying. In the far-field $\tilde{y} > 1$ km, the signals develop similar skewness, with relatively long-temporal tails (Figures 9c–9f). The optimized model D_{IS} curves (dashed red) at each location lag D_{SZ} owing to the exchange time-scale $k_{SZ}^{-1} \approx 2.3$ h. As the surf-zone/inner-shelf exchange terms in Equations 9–10 are proportional to ($D_{SZ} - D_{IS}$), the D_{SZ} skewness is due to the lagged D_{IS} arrival and the time period when $D_{IS} > D_{SZ}$, corresponding to net tracer transport from the inner-shelf to the surf-zone (i.e., recirculation). Model parameter $\gamma = 0.33$ implies a stratified upper limit $L_{IS} \leq A_{SZ}/(\gamma d_{SZ}) = 150$ m, suggesting the model inner-shelf region spans $-250 \leq \tilde{x} < -100$ m. Sparse *in situ* measurements of tracer vertical structure $D(z)$ over this region prevents the use of remotely sensed $D(\tilde{x}, \tilde{y}, t)$ for quantitative assessment of

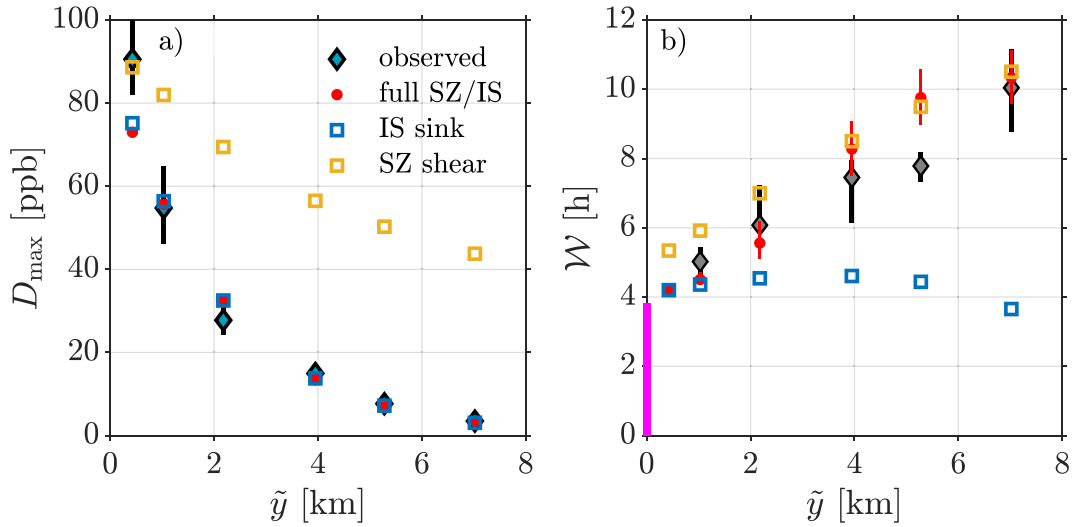

Figure 10. (a) Observed maximum surf-zone dye concentration D_{max} (teal diamonds) and modeled using optimized parameters (red dots, full SZ/IS), the no-recirculation case with $\gamma = 0$ (blue squares, IS sink), and surf-zone shear dispersion case with $k_{SZ} = 0$ (orange squares, SZ shear) vs. alongshore ¡ . (b) Tracer signal duration $\mathcal{W}$ versus ¡ for observations (gray diamonds) and models (same markers) with corresponding ±5% threshold change (error bars) for observations (black) and the fully coupled model (red).

modeled inner-shelf dye D_{IS}. At long-times, the far-field model D_{SZ} curves fall below the minimum detectable signal level before the surf-zone instruments. However, *in situ* measurements ≤1 ppb are likely due to noise. Overall, the signals are consistent, with the D-signal arrival occurring near $(\mathcal{T} - \tilde{y}/v_{SZ}) = 0$.

The bulk surf-zone D and D_{SZ} statistics are also consistent (diamonds vs. red dots, Figure 10). Overall, the decay in maximum concentration D_{max} are very similar, both exhibiting an exponential-like decay with alongshore decay length scale ≈ 1.6 km (teal and red, Figure 10a). The roughly 15 ppb difference in near-field maximum concentration ($\tilde{y} = 0.4$ km) suggests the near-field surf-zone is not well mixed. The modeled dye release instantaneously mixes across the surf-zone, giving $D_{SZ}(\tilde{y} = 0) \sim M/(A_{SZ}\Delta\tilde{y}\mathcal{W}) \approx 96$ ppb, whereas if the near-field is not well mixed (i.e., distributed over cross-sectional area $< A_{SZ}$) then mid-surf-zone *in situ* D measurements may overestimate the surf-zone cross-sectional area averaged concentration. The increasing downstream signal width $\mathcal{W}$ is similar for both observed D and modeled D_{SZ} (Figure 10b). At $\tilde{y} = 1$ km, modeled and observed $\mathcal{W}$ are between 4 and 5 hr. The signal width $\mathcal{W}$ increases to ≈ 10 h at $\tilde{y} = 7$ km. The larger model $\mathcal{W}$ at $\tilde{y} = 5.2$ km is due to a dip in observed $D(\mathcal{T})$ over $7 \le (\mathcal{T} - \tilde{y}/v_{SZ}) \le 10$ h (Figure 9e).

5. Discussion

5.1. The Inner-Shelf Reservoir and Recirculation

The rapid downstream (y) decay in surf-zone maximum concentration D_{max} and the far-field ($y > 1$ km) long-duration tracer signal following passage of the maximum concentration, increasing the signal width $\mathcal{W}$, are well represented by the model (Figures 9a–9f, 10a and 10b). To determine which model terms, and thereby which mechanism, contribute to these aspects of the tracer evolution, two modified tracer evolution equations are examined. First, is a no-recirculation scenario with surf-zone tracer evolution equation,

$$\frac{\partial D_{SZ}^{(1)}}{\partial t} + v_{SZ}\frac{\partial D_{SZ}^{(1)}}{\partial \tilde{y}} = -k_{SZ}^{(1)} D_{SZ}^{(1)} + K_{\tilde{y}\tilde{y}}\frac{\partial^2 D_{SZ}^{(1)}}{\partial \tilde{y}^2} + Q_0\delta(\tilde{y})\Pi(\mathcal{T}), \tag{15}$$

where $k_{SZ}^{(1)} = 3k_{SZ}/4$ is reduced from the optimized parameter used in Equation 9. Equation 15 is essentially equivalent to the fully coupled model (9) and (10) with $\gamma = 0$, thereby making the inner-shelf a perfect sink and neglecting recirculation ($D_{IS}(\tilde{y}, t) = 0$ for all time). For consistency, the no-recirculation model (15) was discretized and time-stepped as discussed in Section 4.

In comparison to the fully coupled surf-zone/inner-shelf model with optimized parameters (red, Figure 10a), the no-recirculation scenario captures the decay in maximum concentration D_{max} with increasing $\tilde{y}$ (blue, Figure 10a). The modified $k_{SZ}^{(1)} = 3k_{SZ}/4$ was determined by minimizing the y-averaged relative error in D_{max}, and is reduced because the optimized k_{SZ} over-estimates the decay in D_{max} for the no-recirculation scenario. In contrast to D_{max}, the far-field no-recirculation signal width $\mathcal{W}$ (blue) differs significantly from the fully coupled model (red, Figure 10b); the fully coupled $\mathcal{W}$ increases continuously (red) while the no-recirculation $\mathcal{W}$ decreases after $\tilde{y} = 4$ km (blue). Both the reduced $k_{SZ}^{(1)}$ and decreasing $\mathcal{W}$ result from assuming the inner-shelf region is a perfect tracer sink. In the fully coupled model, the inner-shelf acts as a reservoir storing tracer that is later recirculated into the surf-zone due to differential advection ($v_{SZ} \neq v_{IS}$), causing the fully coupled $\mathcal{W}$ to increase. Thus, the finite cross-shore extent of inner-shelf tracer plume (i.e., $\gamma \neq 0$), which results in recirculation, is a fundamental component of the observed surf-zone tracer evolution.

Strong cross-shore shear in the surf-zone alongshore current can also cause increasing downstream $\mathcal{W}$, and we evaluate this mechanism using an enhanced surf-zone shear-dispersion scenario, with evolution equation,

$$\frac{\partial D_{SZ}^{(2)}}{\partial t} + v_{SZ}\frac{\partial D_{SZ}^{(2)}}{\partial \tilde{y}} = K_{\tilde{y}\tilde{y}}^{(2)}\frac{\partial^2 D_{SZ}^{(2)}}{\partial \tilde{y}^2} + Q_0\delta(\tilde{y})\Pi(\mathcal{T}), \tag{16}$$

where $K_{\tilde{y}\tilde{y}}^{(2)} = 10K_{\tilde{y}\tilde{y}}$ was determined by minimizing the y-averaged relative error in $\mathcal{W}$. Equation 16 is essentially equivalent to the fully coupled model (9) and (10) with $k_{SZ} = 0$, that is, no surf-zone/inner-shelf exchange. In the surf-zone shear-dispersion scenario, the D_{max} decay is not well represented (orange, Figure 10a). This is partially due to the tracer release having a top-hat structure in time, which due to strong surf-zone advection leads to a broad alongshore region with roughly constant $D_{SZ}^{(2)} \sim M/(A_{SZ}v_{SZ}\mathcal{W}_0)$, thereby decreasing the effectiveness of shear dispersion in reducing D_{max}. The signal width $\mathcal{W}$ at long-distances, over $4 \leq \tilde{y} \leq 7$ km (orange, Figure 10b), is better relative to the no-recirculation scenario (blue), but over estimates $\mathcal{W}$ near the release due to the rapid alongshore spreading following the step-like or discontinuous release start. To roughly match the fully coupled $\mathcal{W}$ growth, an anomalously large $K_{\tilde{y}\tilde{y}}^{(2)} = 10K_{\tilde{y}\tilde{y}}$ was required, indicating intra-surf-zone shear dispersion is not a physically plausible explanation for the growing $\mathcal{W}$.

The surf-zone only shear-dispersion model failure to reproduce the observed plume evolution is consistent with previous observations of dispersion in rivers and estuaries (e.g., Chatwin & Allen, 1985), indicating the physical assumptions of the 1D asymptotic dispersion model are violated (e.g., Young & Jones, 1991). Here, the inter-surf-zone/inner-shelf exchange and recirculation, combined with differential advection, can be considered as a type of shear dispersion across both surf-zone/inner-shelf regions. As inner-shelf mixing strength is weaker than the surf-zone, the time-scale for inner-shelf retention is long, and does not satisfy the theoretical asymptotic requirements. It is possible to achieve comparable D_{max} decay and $\mathcal{W}$ growth by adjusting both $K_{\tilde{y}\tilde{y}}$ and $k_{SZ}^{(1)}$ in Equation 15. However, the required larger model $K_{\tilde{y}\tilde{y}}$ induces a downstream phase shift (earlier $\mathcal{T}_f$ and $\mathcal{T}_p$, not shown), resulting in larger ε, and does not reproduce the signal skewness (long temporal tails). The skill of the fully coupled model indicates that accurately forecasting surf-zone tracer evolution on the time-scales considered here (1–30 hr) requires *a priori* knowledge of the surf-zone and inner-shelf alongshore tracer transport (v_{SZ} and v_{IS}), the relative scales of the surf-zone and inner-shelf (γ), and the exchange rates (k_{SZ} and k_{IS}). On longer time-scales, additional consideration for contributions to k_{IS} from inner-shelf processes are likely needed.

In this study, the fully coupled model parameter ranges were well constrained using observations, and are relatively consistent with existing empirical scalings. For example, the radiation stress based estimate v_{SZ}^{mod} (blue, Figure 7a) was similar to the tracer derived estimates, with best-fit Rayleigh drag coefficient $\mu \approx 2.5 \times 10^{-3}$ m s^{-1} comparable to previous estimates from field observations (Feddersen et al., 1998; Lentz et al., 1999). Similarly, the surf-zone exchange rate $k_{SZ} \sim u_{EX}/L_{SZ}$, was similar to previous estimates of $u_{EX} \approx 1$ cm s^{-1} in similar conditions (e.g., Hally-Rosendahl et al., 2015). Similar long-range observations of shoreline tracer evolution under varying conditions are necessary to examine whether the coupled surf-zone/inner-shelf model and scalings are generalizable. The cross shore decay of TRC-induced u_{EX} is self-similar in models (Suanda & Feddersen, 2015), depending on incident wave and beach conditions, suggesting that TRC contributions to inner-shelf scales L_{IS}, or A_{IS} and k_{IS} are related to wave and beach parameters. However, these inner-shelf parameters also include contributions from many processes distinct from the surf-zone, like winds, alongshore pressure gradients, internal waves, among others. Some of these aspects will be discussed in more detail next.

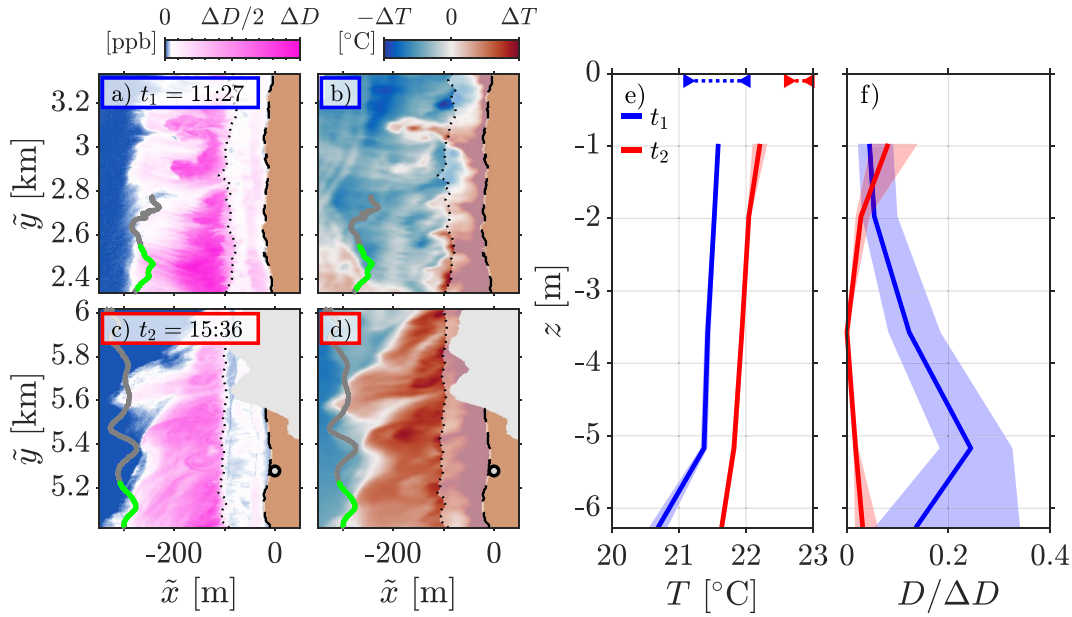

Figure 11. Remotely sensed (a and c) $D(\tilde{x}, \tilde{y})$ and (b and d) long-wave infrared (LWIR) derived relative temperature $T'(\tilde{x}, \tilde{y})$, relative to the alongshore and $-250 \le \tilde{x} \le -200$ m average, at local times (a and b) t_1 = 11:27 and (c and d) t_2 = 15:36. Alongshore domains are roughly centered on $\tilde{y} = \tilde{y}_f - 1.5$ km, corresponding to the front position $\tilde{y}_f$ one surf-zone flushing period earlier $k_{SZ}^{-1} = 2.3$ h, or $v_{SZ}/k_{SZ} = 1.5$ km (Figures 4 and 7a). Color scales (a) $\Delta D = 20$ ppb and (c) $\Delta D = 10$ ppb account for decreasing downstream D_{max} (Figure 7b); and LWIR temperature T' is relative to the $-250 \le \tilde{x} \le -200$ m and 1 km alongshore average and color scales (b) $\Delta T = 0.15$°C and (d) $\Delta T = 0.4$°C account for increasing surf-zone/inner-shelf temperature anomaly. Vertical profiles of 5 min averaged inner-shelf (e) $T(z)$ and (f) non-dimensional $D(z)/\Delta D$. Solid vertical profiles are averaged along the green segments (a-d), and transparent shading indicates ±1 standard deviation from the mean. At the top of (a) are the alongshore averaged surf-zone temperature ranges over the $k_{SZ}^{-1} = 2.3$ h period prior to t_1 (blue) and t_2 (red), respectively.

5.2. Processes Affecting Inner-Shelf Tracer Evolution

Inner-shelf tracer evolution is affected by various processes ranging from surf-zone origin transient rip-currents (Hally-Rosendahl et al., 2015) to stratified dynamics, such as internal waves (Grimes, Feddersen, Giddings, & Pawlak, 2020; Omand et al., 2011) and cross-shore buoyancy gradients (Grimes, Feddersen, & Kumar, 2020; Moulton et al., 2021). However, the fully coupled surf-zone/inner-shelf tracer model does not distinguish between specific process contributions to γ or k_{IS}; nor whether the inner-shelf region is vertically well mixed or stratified (cross-hatch patterns in Figure 8). Here, morning and afternoon (t_1 = 11:27 and t_2 = 15:36 local time, respectively) remotely sensed inner-shelf dye $D(\tilde{x}, ty)$ and surface perturbation temperature $T'(\tilde{x}, \tilde{y})$ are combined with *in situ* $D(z)$ and $T(z)$ profiles to illustrate some affects of stratified inner-shelf processes on tracer evolution (Figure 11).

Remotely sensed D and T' domains are roughly centered $v_{SZ}/k_{SZ} = 1.5$ km south of $\tilde{y}_f$ (red ×, Figure 4), that is, the location of the northward propagating front $\tilde{y}_f$ one surf-zone flushing period $k_{SZ}^{-1} \approx 2.3$ h prior. The shifted domain concentration ranges $\Delta D_1 = 20$ and $\Delta D_2 = 10$ ppb roughly correspond to the respective $D_{max}(\tilde{y})$ (cf. Figure 7b), for example, the instrument in Figure 11c at t_2 = 15:36 corresponds to $\mathcal{T} = 10.3$ h in Figure 6e. Vertical profiles of 5 min averaged inner-shelf $T(z)$ and non-dimensional $D(z)/\Delta D$ were taken from alongshore vessel transects in each of the remotely sensed domains (green segments in Figures 11a–11d).

In the remotely sensed $D(\tilde{x}, \tilde{y})$, there are active rip-current ejections, with D comparable to D_{max} (e.g., $\tilde{y} \approx 3.1$ km, Figure 11a) and a more diffuse larger-scale underlying D indicating continuous horizontal mixing of previous rip-current ejection events over the preceding 2.3 hr (Figures 11a and 11c). Rip-current ejections are also evident in remotely sensed T' (Figures 11b and 11d). However, the cross-shore extent of morning warm T' plumes is notably smaller than the afternoon. Also, the morning diffuse inner-shelf D does not have strong coherence with T' (Figures 11a and 11b), in contrast to mid-afternoon inner-shelf D and T' (Figures 11c and 11d) when

surf-zone/inner-shelf temperature anomaly ΔT is a factor of 2 larger. Recent observations and modeling suggest that a larger surf-zone/inner-shelf temperature anomaly (ΔT) induce larger cross-shore surface extent of rip-current thermal plumes (Moulton et al., 2021).

At $\tilde{x} \approx -300$ m (outside the model inner-shelf region), vertical profiles of inner-shelf $T(z)$ and non-dimensional $D(z)/\Delta D$ indicate different morning and afternoon inner-shelf D evolution (Figures 11e and 11f). The inner-shelf $T(z)$ is roughly 0.5 °C warmer in the afternoon (red vs. blue, Figure 11e), with increased near-surface stratification. Profiles of morning versus afternoon $D(z)/\Delta D$ have notably different vertical structure (Figure 11f). The morning $D(z)/\Delta D_1$ has a subsurface maximum at $z \approx -5$ m (blue), with strong temporal variability (shading) relative to afternoon. The afternoon $D(z)/\Delta D_2$ is near-surface maximum and relatively weak mid water column (red), suggesting different inner-shelf tracer evolution over the $k_{SZ}^{-1} = 2.3$ h prior to each image and transect.

Prior to the mid-morning transect, the alongshore averaged surf-zone temperature (blue left/right triangles, top of Figure 11e) overlapped the inner-shelf temperature $T(z)$ for $z \geq -5$ m. Thus, tracer exported onto the inner-shelf over the morning could be transported offshore subsurface beyond $\tilde{x} = -(L_{SZ} + L_{IS})$. This time-period also corresponded to the local internal tide driven 300 m cross-shore deformation of the inner-shelf plume ($\tilde{y} \leq 2$ km, Figures 4a and 4b), which potentially subducted the dye-laden water mass (Grimes, Feddersen, Giddings, & Pawlak, 2020). As remotely sensed D is an average measure of tracer within the optical depth of the water column, some of the mid-morning diffuse underlying D signal (Figures 11a) is potentially due to subsurface tracer.

In contrast, the afternoon period alongshore averaged surf-zone (red triangles, top of Figures 11e) was consistently 0.5°C warmer than the $z \approx -1$ m inner-shelf T. Surf-zone tracer exported onto the inner-shelf with positive T-anomaly would preferentially spread offshore at, or near the surface due to buoyancy (e.g., Molina et al., 2014; Moulton et al., 2021). In idealized modeling studies, diurnal thermally driven circulation modulates the inner-shelf vertical distribution of surf-zone released tracers, with a near surface inner-shelf plume for warm surf-zones and sub-surface plume for cool surf-zones (Grimes, Feddersen, & Kumar, 2020). Although the coupled model with constant γ and $k_{IS} \approx k_{SZ}/2$ reproduced the overall surf-zone tracer evolution, both the internal tide and solar heating contributed to the inner-shelf D evolution, making a process-based generalization of inner-shelf cross-shore exchange rate (i.e., k_{IS}) impossible from a single realization.

6. Summary

The evolution of an early morning surf-zone released fluorescent tracer was observed for ≈ 30 h after release using aerial imagery and *in situ* sampling. Surf-zone tracer was advected north throughout the observation period with tracer transport derived mean speed of $v_{SZ} \approx 0.18$ m s^{-1}, based on surf-zone instrument arrival times and remote inner-shelf surface plume position, consistent with the obliquely incident wave forcing. Downstream of the release ($\tilde{y} > 0$), the maximum *in situ* surf-zone tracer concentration D_{max} decayed exponentially with 1.6 km alongshore e-folding length scale, or 2.5 hr advective time scale. Downstream surf-zone tracer time-series also evolved, having top-hat structure for $y \leq 1$ km and becoming increasingly skewed farther downstream. Within ≈ 1.5 km of the northward propagating tracer front, inner-shelf tracer was confined to onshore of $4L_{SZ}$ (surf-zone width $L_{SZ} \approx 100$ m) and was alongshore patchy.

A coupled surf-zone/inner-shelf box tracer model generally reproduces the observed surf-zone tracer evolution. The model accounts for surf-zone/inner-shelf alongshore advection (v_{SZ} and v_{IS}, respectively), surf-zone shear dispersion ($K_{\tilde{y}\tilde{y}}$), and cross-shore tracer exchange across the surf-zone and inner-shelf (k_{SZ} and k_{IS}, respectively). The downstream D_{max} decay is largely due to rip-current ejections of tracer, leading to alongshore patchy inner-shelf dye, and parameterized using a surf-zone exchange rate k_{SZ}, implying a surf-zone flushing time $k_{SZ}^{-1} \approx 2.3$ h. Inner-shelf exchange was weaker, $k_{IS} \approx k_{SZ}/2$, indicating reduced horizontal mixing. The surf-zone exchange rate k_{SZ} magnitude is consistent with previous estimates in similar conditions, and the cross-shore decay in exchange is consistent with previous model simulations of mixing due to surf-zone generated transient rip-currents. The observed growth of downstream D temporal skewness is due to inner-shelf D retention, differential surf-zone/inner-shelf advection ($v_{SZ} \neq v_{IS}$), and subsequent surf-zone recirculation. The growth of downstream D temporal width, an indication of growing alongshore plume width, was not well represented by a 1D asymptotic shear dispersion model, likely due to cross-shore inhomogeneous mixing and long inner-shelf exchange time scale, that is, $k_{IS}^{-1} \approx 6$ h.

Contributions to model parameters from surf-zone processes were well constrained by observations and consistent with existing scalings. The inner-shelf D evolution exhibited more complexity, owing to multiple overlapping processes. On the inner-shelf ($\approx 3L_{SZ}$) for $\tilde{y} > 2$ km, tracer vertical structure differed in the morning versus afternoon, with mid-morning $D(z)$ largely sub-surface and afternoon $D(z)$ confined to the surface. The different tracer structure is likely due to surf-zone/inner-shelf temperature differences, with similar mid-morning surf-zone/inner-shelf temperature allowing for subsurface tracer exchange, in contrast to the warmer afternoon surf-zone leading to buoyant near-surface inner-shelf tracer. The mid-morning evolution was also likely affected by the local internal tide circulation. Scalings for various other inner-shelf exchange processes (i.e., k_{IS}), like internal tides, waves, and buoyancy driven circulation are required to generalize the coupled model.

Data Availability Statement

Data was made available in part by SIO CDIP, and the Tijuana River National Estuary Research Reserve and are available through the UCSD Digital Library at https://doi.org/10.6075/J02F7NBJ (Grimes et al., 2021) or by contacting the corresponding author. The U.S. Navy provided access to Navy property for data collection. We thank Ken Melville, Luc Lenain, Nick Statom, and Stephen Holleman for acquisition and preliminary processing of MASS data; and Elizabeth Brasseale for thoughtful discussions about surf-zone tracer evolution. We thank YMCA: Camp Surf for providing a base of operations; the cities of Imperial Beach and Coronado, the US Navy and CA State Parks for accommodating our research activities; and the numerous Imperial Beach lifeguards, UCSD/SIO students, and volunteers for efforts to keep beachgoers safe and monitor surf-zone instrumentation.

Acknowledgments
This work was funded under the CSIDE grant by the National Science Foundation (NSF OCE-1459389). This work was also supported by the Office of Naval Research through grant N00014-5-1-2631. This project was also supported, in part, by the US Coastal Research Program (USCRP) as administered by the US Army Corps of Engineers (USACE), Department of Defense and in part by NSF OCE-1924005. The content of the information provided in this publication does not necessarily reflect the position or the policy of the government, and no official endorsement should be inferred. The authors' acknowledge the USACE and USCRP's support of their effort to strengthen coastal academic programs and address coastal community needs in the United States.

References

Austin, J. A., & Lentz, S. J. (2002). The inner shelf response to wind-driven upwelling and downwelling. *Journal of Physical Oceanography*, *32*(7), 2171–2193.

Boehm, A. B. (2003). Model of microbial transport and inactivation in the surf zone and application to field measurements of total coliform in northern orange county, California. *Environmental Science & Technology*, *37*(24), 5511–5517. https://doi.org/10.1021/es034321x

Boehm, A. B., Ismail, N. S., Sassoubre, L. M., & Andruszkiewicz, E. A. (2017). Oceans in Peril: Grand challenges in applied water quality research for the 21st century. *Environmental Engineering Science*, *34*(1), 3–15. https://doi.org/10.1089/ees.2015.0252

Brown, J. A., MacMahan, J. H., Reniers, A. J. H. M., & Thornton, E. B. (2015). Field observations of surf zone-inner shelf exchange on a rip-channeled beach. *Journal of Physical Oceanography*, *45*(9), 2339–2355. https://doi.org/10.1175/JPO-D-14-0118.1

Brown, J. A., MacMahan, J. H., Reniers, A. J. H. M., Thornton, E. B., Shanks, A. L., Morgan, S. G., & Gallagher, E. L. (2019). Observations of mixing and transport on a steep beach. *Continental Shelf Research*, *178*, 1–14. https://doi.org/10.1016/j.csr.2019.03.009

Chatwin, P. C. (1971). On the interpretation of some longitudinal dispersion experiments. *Journal of Fluid Mechanics*, *48*(4), 689–702. https://doi.org/10.1017/S0022112071001800

Chatwin, P. C., & Allen, C. M. (1985). Mathematical models of dispersion in rivers and estuaries. *Annual Review of Fluid Mechanics*, *17*(1), 119–149. https://doi.org/10.1146/annurev.fl.17.010185.001003

Chikwendu, S. C., & Ojiakor, G. U. (1985). Slow-zone model for longitudinal dispersion in two-dimensional shear flows. *Journal of Fluid Mechanics*, *152*, 15–38. https://doi.org/10.1017/S0022112085000544

Clark, D. B., Elgar, S., & Raubenheimer, B. (2012). Vorticity generation by short-crested wave breaking. *Geophysical Research Letters*, *39*(24). https://doi.org/10.1029/2012GL054034

Clark, D. B., Feddersen, F., & Guza, R. T. (2010). Cross-shore surfzone tracer dispersion in an alongshore current. *Journal of Geophysical Research: Oceans*, *115*(C10), C10035. https://doi.org/10.1029/2009JC005683

Clark, D. B., Feddersen, F., Omand, M. M., & Guza, R. T. (2009). Measuring fluorescent dye in the bubbly and sediment-laden surfzone. Water. *Air and Soil Pollution*, *11204*(1–4), 103–115.

Clark, D. B., Lenain, L., Feddersen, F., Boss, E., & Guza, R. T. (2014). Aerial imaging of fluorescent dye in the near shore. *Journal of Atmospheric and Oceanic Technology*, *31*(6), 1410–1421. https://doi.org/10.1007/s11270-009-0030-z

Clarke, L., Ackerman, D., & Largier, J. (2007). Dye dispersion in the surf zone: Measurements and simple models. *Continental Shelf Research*, *27*(5), 650–669. https://doi.org/10.1016/j.csr.2006.10.010

Elder, J. W. (1959). The dispersion of marked fluid in turbulent shear flow. *Journal of Fluid Mechanics*, *5*(4), 544–560. https://doi.org/10.1017/S0022112059000374

Feddersen, F. (2014). The generation of surfzone eddies in a strong alongshore current. *Journal of Physical Oceanography*, *44*, 600–617. https://doi.org/10.1175/JPO-D-13-051.1

Feddersen, F., Guza, R. T., Elgar, S., & Herbers, T. H. C. (1998). Alongshore momentum balances in the nearshore. *Journal of Geophysical Research: Oceans*, *103*(C8), 15667–15676. https://doi.org/10.1029/98JC01270

Feddersen, F., Guza, R. T., Elgar, S., & Herbers, T. H. C. (2000). Velocity moments in alongshore bottom stress parameterizations. *Journal of Geophysical Research: Oceans*, *105*(C4), 8673–8686. https://doi.org/10.1029/2000JC900022

Feddersen, F., Olabarrieta, M., Guza, R. T., Winters, D., Raubenheimer, B., & Elgar, S. (2016). Observations and modeling of a tidal inlet dye tracer plume. *Journal of Geophysical Research: Oceans*, *121*, 7819–7844. https://doi.org/10.1002/2016JC011922

Fong, D. A., & Stacey, M. T. (2003). Horizontal dispersion of a near-bed coastal plume. *Journal of Fluid Mechanics*, *489*, 239–267.

Frouin, R., Schwindling, M., & Deschamps, P.-Y. (1996). Spectral reflectance of sea foam in the visible and near-infrared: In situ measurements and remote sensing implications. *Journal of Geophysical Research*, *101*(C6), 14361–14371. https://doi.org/10.1017/s002211200300510x

Geiman, J. D., Kirby, J. T., Reniers, A. J. H. M., & MacMahan, J. H. (2011). Effects of wave averaging on estimates of fluid mixing in the surf zone. *Journal of Geophysical Research*, *116*(C4). https://doi.org/10.1029/2010JC006678

Grant, S. B., Kim, J. H., Jones, B. H., Jenkins, S. A., Wasyl, J., & Cudaback, C. (2005). Surf zone entrainment, along-shore transport, and human health implications of pollution from tidal outlets. *Journal of Geophysical Research*, *110*, C10025. https://doi.org/10.1029/2004JC002401

Grimes, D. J., Feddersen, F., & Giddings, S. N. (2021). Data from: Surf-zone tracer alongshore transport and dilution due to oblique waves, rip-currents, and inner-shelf recirculation over long-distance/time. In *The cross-surfzone/inner-shelf dye exchange (CSIDE) study*. UC San Diego Library Digital Collections. https://doi.org/10.6075/J02F7NBJ

Grimes, D. J., Feddersen, F., Giddings, S. N., & Pawlak, G. (2020). Cross-shore deformation of a surfzone-released dye plume by an internal tide on the inner shelf. *Journal of Physical Oceanography*, *50*(1), 35–54. https://doi.org/10.1175/JPO-D-19-0046.1

Grimes, D. J., Feddersen, F., & Kumar, N. (2020). Tracer exchange across the stratified inner-shelf driven by transient rip-currents and diurnal surface heat fluxes. *Geophysical Research Letters*, *47*(10). https://doi.org/10.1029/2019GL086501

Hally-Rosendahl, K., Feddersen, F., Clark, D. B., & Guza, R. T. (2015). Surfzone to inner-shelf exchange estimated from dye tracer balances. *Journal of Geophysical Research: Oceans*, *120*(9), 6289–6308. https://doi.org/10.1002/2015JC010844

Hally-Rosendahl, K., Feddersen, F., & Guza, R. T. (2014). Cross-shore tracer exchange between the surfzone and inner-shelf. *Journal of Geophysical Research: Oceans*, *119*(7), 4367–4388. https://doi.org/10.1002/2013JC009722

Harris, T. F. W., Jordaan, J. M., McMurray, W. R., Verwey, C. J., & Anderson, F. P. (1963). Mixing in the surf zone. *International Journal of Air and Water Pollution*, *7*, 649–652.

Johnson, D., & Pattiaratchi, C. (2006). Boussinesq modelling of transient rip currents. *Coastal Engineering*, *53*(5), 419–439. https://doi.org/10.1016/0926-6569(63)90186-x

Jones, N. L., Lowe, R. J., Pawlak, G., Fong, D. A., & Monismith, S. G. (2008). Plume dispersion on a fringing coral reef system. *Limnology & Oceanography*, *53*(5part2), 2273–2286. https://doi.org/10.4319/lo.2008.53.5_part_2.2273

Kastner, S. E., Horner-Devine, A. R., & Thomson, J. M. (2019). A conceptual model of a river plume in the surf zone. *Journal of Geophysical Research: Oceans*, *124*(11), 8060–8078. https://doi.org/10.1029/2019JC015510

Kirkpatrick, B., Pierce, R., Cheng, Y. S., Henry, M. S., Blum, P., Osborn, S., et al. (2010). Inland transport of aerosolized florida red tide toxins. *Harmful Algae*, *9*, 186–189. https://doi.org/10.1016/j.hal.2009.09.003

Kumar, N., & Feddersen, F. (2017). The effect of Stokes drift and transient rip currents on the inner shelf. part ii: With stratification. *Journal of Physical Oceanography*, *47*(1), 243–260. https://doi.org/10.1175/JPO-D-16-0077.1

Lentz, S. J., & Fewings, M. R. (2012). The wind- and wave-driven inner-shelf circulation. *Annual Review of Marine Science*, *4*(1), 317–343. https://doi.org/10.1146/annurev-marine-120709-142745

Lentz, S. J., Guza, R. T., Elgar, S., Feddersen, F., & Herbers, T. H. C. (1999). Momentum balances on the North Carolina inner shelf. *Journal of Geophysical Research: Oceans*, *104*(C8), 18205–18226. https://doi.org/10.1029/1999JC900101

Longuet-Higgins, M. S. (1970). Longshore currents generated by obliquely incident sea waves: 1. *Journal of Geophysical Research*, *75*(33), 6778–6789. https://doi.org/10.1029/JC075i033p06778

Melville, W. K., Lenain, L., Cayan, D. R., Kahru, M., Kleissl, J. P., Linden, P. F., & Statom, N. M. (2016). The modular aerial sensing system. *Journal of Atmospheric and Oceanic Technology*, *33*(6), 1169–1184. https://doi.org/10.1175/JTECH-D-15-0067.1

Molina, L., Pawlak, G., Wells, J. R., Monismith, S. G., & Merrifield, M. A. (2014). Diurnal cross-shore thermal exchange on a tropical forereef. *Journal of Geophysical Research: Oceans*, *119*(9), 6101–6120. https://doi.org/10.1002/2013JC009621

Moniz, R. J., Fong, D. A., Woodson, C. B., Willis, S. K., Stacey, M. T., & Monismith, S. G. (2014). Scale-dependent dispersion within the stratified interior on the shelf of northern monterey bay. *Journal of Physical Oceanography*, *44*(4), 1049–1064. https://doi.org/10.1175/JPO-D-12-0229.1

Morgan, S. G., Shanks, A. L., MacMahan, J. H., Reniers, A. J., & Feddersen, F. (2018). Planktonic subsidies to surf-zone and intertidal communities. *Annual Review of Marine Science*, *10*(1), 345–369. https://doi.org/10.1146/annurev-marine-010816-060514

Moulton, M., Chickadel, C. C., & Thomson, J. (2021). Warm and cool nearshore plumes connecting the surf zone to the inner shelf. *Geophysical Research Letters*, *48*, e2020GL091675. https://doi.org/10.1029/2020GL091675

Omand, M. M., Leichter, J. J., Franks, P. J. S., Guza, R. T., Lucas, A. J., & Feddersen, F. (2011). Physical and biological processes underlying the sudden surface appearance of a red tide in the nearshore. *Limnology & Oceanography*, *56*(3), 787–801. https://doi.org/10.4319/lo.2011.56.3.0787

Pendergraft, M. A., Grimes, D. J., Giddings, S. N., Feddersen, F., Beall, C. M., Lee, C., et al. (2021). Airborne transmission pathway for coastal water pollution. *PeerJ*, *9*, e11358. https://doi.org/10.7717/peerj.11358

Peregrine, D. (1998). Surf zone currents. *Theoretical and Computational Fluid Dynamics*, *10*(1), 295–309. https://doi.org/10.1007/s001620050065

Reniers, A. J. H. M., MacMahan, J. H., Beron-Vera, F. J., & Olascoaga, M. J. (2010). Rip-current pulses tied to lagrangian coherent structures. *Geophysical Research Letters*, *37*(5). https://doi.org/10.1029/2009GL041443

Reniers, A. J. H. M., MacMahan, J. H., Thornton, E. B., Stanton, T. P., Henriquez, M., Brown, J. W., et al. (2009). Surf zone surface retention on a rip-channeled beach. *Journal of Geophysical Research*, *114*(C10). https://doi.org/10.1029/2008JC005153

Rodriguez, A. R., Giddings, S. N., & Kumar, N. (2018). Impacts of nearshore wave-current interaction on transport and mixing of small-scale buoyant plumes. *Geophysical Research Letters*, *45*(16), 8379–8389. https://doi.org/10.1029/2018GL078328

Roe, P. L. (1986). Characteristic-based schemes for the Euler equations. *Annual Review of Fluid Mechanics*, *18*(1), 337–365. https://doi.org/10.1146/annurev.fl.18.010186.002005

Sinnett, G., & Feddersen, F. (2016). Observations and parameterizations of surfzone albedo. *Methods in Oceanography*, *17*, 319–334. (Special section on Novel instrumentation in Oceanography: a dedication to Rob Pinkel). https://doi.org/10.1016/j.mio.2016.07.001

Spydell, M. S., & Feddersen, F. (2012a). The effect of a non-zero lagrangian time scale on bounded shear dispersion. *Journal of Fluid Mechanics*, *691*, 69–94. https://doi.org/10.1017/jfm.2011.443

Spydell, M. S., & Feddersen, F. (2012b). A lagrangian stochastic model of surf zone drifter dispersion. *Journal of Geophysical Research*, *117*(C3). https://doi.org/10.1029/2011JC007701

Spydell, M. S., Feddersen, F., & Guza, R. T. (2009). Observations of drifter dispersion in the surfzone: The effect of sheared alongshore currents. *Journal of Geophysical Research*, *114*(C7). https://doi.org/10.1029/2009JC005328

Spydell, M. S., Feddersen, F., & Suanda, S. (2019). Inhomogeneous turbulent dispersion across the nearshore induced by surfzone eddies. *Journal of Physical Oceanography*, *49*(4), 1015–1034. https://doi.org/10.1175/JPO-D-18-0102.1

Suanda, S. H., & Feddersen, F. (2015). A self-similar scaling for cross-shelf exchange driven by transient rip currents. *Geophysical Research Letters*, *42*(13), 5427–5434. https://doi.org/10.1002/2015GL063944

Sundermeyer, M. A., & Ledwell, J. R. (2001). Lateral dispersion over the continental shelf: Analysis of dye release experiments. *Journal of Geophysical Research: Oceans*, *106*(C5), 9603–9621. https://doi.org/10.1029/2000JC900138

Taylor, G. I. (1954). The dispersion of matter in turbulent flow through a pipe. *Proceedings of the Royal Society of London - Series A: Mathematical and Physical Sciences*, *223*(1155), 446–468. https://doi.org/10.1098/rspa.1954.0130

Vos, K., Harley, M. D., Splinter, K. D., Simmons, J. A., & Turner, I. L. (2019). Sub-annual to multi-decadal shoreline variability from publicly available satellite imagery. *Coastal Engineering*, *150*, 160–174. https://doi.org/10.1016/j.coastaleng.2019.04.004

Wong, S. H. C., Monismith, S. G., & Boehm, A. B. (2013). Simple estimate of entrainment rate of pollutants from a coastal discharge into the surf zone. *Environmental Science & Technology*, *47*(20), 11554–11561. (PMID: 24006887). https://doi.org/10.1021/es402492f

Wu, X., Feddersen, F., & Giddings, S. N. (2021). Diagnosing surfzone impacts on inner-shelf flow spatial variability using realistic model experiments with and without surface gravity waves. *Journal of Physical Oceanography*. https://doi.org/10.1175/JPO-D-20-0324.1

Wu, X., Feddersen, F., Giddings, S. N., Kumar, N., & Gopalakrishnan, G. (2020). Mechanisms of mid- to outer-shelf transport of shoreline-released tracers. *Journal of Physical Oceanography*, *50*(7), 1813–1837. https://doi.org/10.1175/JPO-D-19-0225.1

Young, W. R., & Jones, S. (1991). Shear dispersion. *Physics of Fluids A: Fluid Dynamics*, *3*(5), 1087–1101. https://doi.org/10.1063/1.858090